Research Square

Preprints are preliminary reports that have not undergone peer review.
They should not be considered conclusive, used to inform clinical practice,
or referenced by the media as validated information.

# A Phospholipid Synthesis Inhibitor Protects Against Bacterial Infection

**Dianfan Li**

lidf9@mail.sysu.edu.cn

School of Agriculture and Biotechnology, Sun Yat-sen University https://orcid.org/0000-0003-4729-4678

**Zhihao Yue**

School of Agriculture and Biotechnology, Sun Yat-sen University

**Yiran Wu**

ShanghaiTech University https://orcid.org/0000-0001-6790-7473

**Tao Zhang**

Shanghai Institute of Materia Medica https://orcid.org/0000-0003-3287-4629

**Hao Xia**

State Key Laboratory of Molecular Biology, Shanghai Institute of Biochemistry and Cell Biology, Center for Excellence in Molecule Cell Science, Chinese Academy of Sciences

**Yannan Tang**

Center for Excellence in Molecular Cell Science, Shanghai Institute of Biochemistry and Cell Biology, Chinese Academy of Sciences, Shanghai, China.

**Zhaowen Shen**

School of Agriculture and Biotechnology, Sun Yat-sen University

**Yihui Pan**

Shanghai Institute of Material Medica, Chinese Academy of Sciences, Shanghai

**Yiheng Li**

School of Chinese Materia Medica, Nanjing University of Chinese Medicine, Nanjing

**Tingting Li**

School of Agriculture and Biotechnology, Sun Yat-sen University

**Kyeong Kyu Kim**

Sungkyunkwan University https://orcid.org/0000-0003-2515-8894

**Cai-Guang Yang**

Shanghai Institute of Materia Medica, Chinese Academy of Sciences https://orcid.org/0000-0001-5778-4422

**Suwen Zhao**

ShanghaiTech University https://orcid.org/0000-0001-5609-434X

**Biological Sciences - Article**

**Keywords:**

**Posted Date:** August 31st, 2026

**DOI:** https://doi.org/10.21203/rs.3.rs-10384816/v1

**License:** This work is licensed under a Creative Commons Attribution 4.0 International License.
Read Full License

**Additional Declarations: Yes** there is potential Competing Interest. D.L., Z.Y., S.Z., and Y.W. are named inventors on a patent application (#2026106446983) related to Gpatin submitted to the Chinese Patent Office by Sun Yat-sen University and ShanghaiTech University.

# Title: A Phospholipid Synthesis Inhibitor Protects Against Bacterial Infection

**Authors:** Zhihao Yue[1,†], Yiran Wsu[2,†], Tao Zhang[3,4,†], Hao Xia[5], Yannan Tang[5], Zhaowen Shen[2], Yihui Pan[3,4], Yiheng Li[6], Tingting Li[1], Kyeong Kyu Kim[7], Cai-Guang Yang[3,4,6,*], Suwen Zhao[2,*], Dianfan Li[1,*]

**Affiliations:**

[1]School of Agriculture and Biotechnology, Sun Yat-sen University, Shenzhen, 518107, China.

[2]School of Life Sciences, ShanghaiTech University, Shanghai, China.

[3]Shanghai Institute of Material Medica, Chinese Academy of Sciences, Shanghai, China.

[4]University of Chinese Academy of Sciences, Beijing, China

[5]Center for Excellence in Molecular Cell Science, Shanghai Institute of Biochemistry and Cell Biology, Chinese Academy of Sciences, Shanghai, China.

[6]School of Chinese Materia Medica, Nanjing University of Chinese Medicine, Nanjing, China

[7]Sungkyunkwan University School of Medicine, Suwon, Korea.

[†]Equal contribution.

[*]Correspondence: yangcg@simm.ac.cn; zhaosw@shanghaitech.edu.cn; lidf9@mail.sysu.edu.cn

**ABSTRACT**

The rapid emergence of multidrug-resistant (MDR) bacteria highlights the urgent need for antibacterial agents that operate through previously unexplored mechanisms. PlsY, a seven-transmembrane glycerol-3-phosphate acyltransferase that catalyzes an essential step in bacterial phospholipid biosynthesis, represents an attractive antibacterial target. However, inhibitor development has so far focused on substrate analogues. Here, we identify Gpatin, a small-molecule inhibitor of PlsY, through structure-based virtual screening and biochemical characterization. Gpatin inhibits PlsY enzymes from multiple pathogenic bacteria and displays antibacterial activity across clinically relevant Gram-positive pathogens, including methicillin-resistant *Staphylococcus aureus* and *Streptococcus pneumoniae*. Cryo-electron microscopy reveals that Gpatin binds within a partially membrane-exposed pocket formed by the C-terminal transmembrane bundle and surrounding phospholipids, overlapping the substrate-binding site and explaining its competitive inhibitory activity. Moreover, Gpatin binding induces a large-scale rearrangement of the transmembrane architecture that disrupts formation of the catalytic phosphate hole required for catalysis, thereby stabilizing PlsY in an inactive conformation. In murine infection models, Gpatin exhibits *in vivo* antibacterial activity against *S. aureus* and *S. pneumoniae*. Together, our findings further establish PlsY as a chemically tractable antibacterial target and reveal an unexpected conformational vulnerability that can be exploited for inhibitor development.

## INTRODUCTION

*Staphylococcus aureus* and *Streptococcus pneumoniae* are among the most clinically important Gram-positive bacterial pathogens, causing skin and soft tissue infections, pneumonia, and invasive diseases[1-3].The emergence of methicillin-resistant *S. aureus* (MRSA)[4,5] and increasing resistance of *S. pneumoniae* to frontline antibiotics[6] have substantially reduced treatment options. Despite recent advances in antibacterial development[7-21], infections caused by these pathogens remain associated with considerable morbidity, mortality, and healthcare costs worldwide[3]. Reflecting their clinical importance, the World Health Organization (WHO) designates *S. aureus* and *S. pneumoniae* as high- and medium-priority bacterial pathogens[22], respectively, while the Centers for Disease Control and Prevention (CDC) lists Group A *Streptococcus* (*S. pyogenes*) as a pathogen of concern[23]. These challenges underscore the need for antibacterial agents with new mechanisms of action.

Bacterial membrane phospholipids are indispensable for membrane biogenesis and numerous cellular processes, making their biosynthetic pathways attractive targets for antibacterial development[24-26]. The clinical advancement of inhibitors targeting type II fatty acid synthesis illustrates the therapeutic potential of bacterial lipid metabolism[25,27-29], whereas phospholipid biosynthesis itself remains comparatively underexplored. Because several enzymes in this pathway are absent from mammalian cells[30], it offers attractive opportunities for selective antibacterial intervention.

PlsY is a membrane-embedded glycerol-3-phosphate acyltransferase (GPAT) that catalyzes the committed step of bacterial phospholipid biosynthesis, producing lysophosphatidic acid (**Fig. S1a**)[31,32]. In Gram-positive bacteria, PlsY serves as the sole GPAT responsible for this essential reaction[31,33]. Unlike canonical GPATs, PlsY shares no detectable sequence homology with other acyltransferase families and utilizes the unusual metabolite acyl-phosphate (acylP) rather than acyl-CoA or acyl-acyl carrier protein as its acyl donor[31]. Mammalian cells lack PlsY homologues,

making this enzyme an attractive target for selective antibacterial development. Previous studies identified acyl-phosphate analogues, including acyl sulfates, that inhibit *S. aureus* growth by targeting PlsY[34,35], providing proof of principle that the enzyme is chemically tractable while leaving the structural basis of inhibition unresolved.

Previously, we determined five high-resolution crystal structures of *Aquifex aeolicus* PlsY (*Aa*PlsY) representing substrate- and product-bound states[36]. Consistent with its unique evolutionary origin, *Aa*PlsY adopts a seven-transmembrane architecture with no structural homology to known protein folds. These structures revealed an unusual catalytic "phosphate hole" formed by a conserved histidine residue and two intramembrane positive helical dipoles, which mediates substrate recognition and stabilizes the negatively charged transition state during substrate-assisted catalysis. These structural insights provided a foundation for structure-based discovery of PlsY inhibitors.

Here, we identify Gpatin (GPAT inhibitor), a small-molecule PlsY inhibitor discovered by structure-based virtual screening. Gpatin inhibits PlsY enzymes from multiple Gram-positive bacterial species and exhibits antibacterial activity against clinically relevant pathogens, including MRSA, *S. pneumoniae*, and *S. pyogenes*. Biochemical analyses demonstrate that Gpatin competitively inhibits PlsY, while cryo-electron microscopy (cryo-EM) reveals that it occupies the substrate-binding region and induces an unexpected conformational rearrangement that disrupts formation of the catalytic phosphate hole, thereby stabilizing PlsY in a catalytically incompetent state. Gpatin also show antibacterial activity in murine models of *S. aureus* skin infection and *S. pneumoniae* pneumonia. Together, our findings define a previously unrecognized conformational vulnerability of PlsY and provide a structural framework for the development of PlsY-targeting antibacterial agents.

## RESULTS

### Identification of PlsY inhibitors

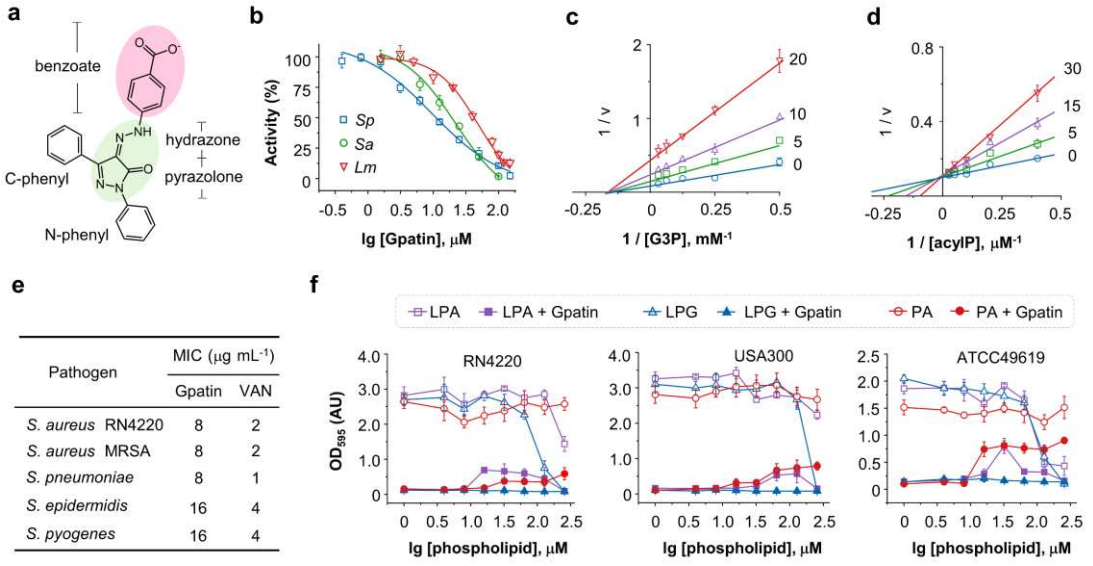
We performed virtual screening of ~1.6 million compounds from the ChemDiv library against structural models of *S. pneumoniae* PlsY in G3P-bound and acylP-bound states. Compounds were manually selected for experimental testing from the top 5,000-ranked candidates for each model. Biochemical screening of 81 selected compounds (**Table S1, Fig. S2a**) identified 5 molecules that inhibited PlsY activity by more than 50% at 20 μM.

To further explore these chemical scaffolds, we sourced an additional 63 analogs based on structural similarity to the top hits (**Table S1**). Ten compounds showed inhibition of more than 50%. Among these, Gpatin (GPAT inhibitor) (**Fig. 1a**) was selected for detailed characterization (**Fig. S2b**).

Gpatin inhibited *Sp*PlsY and *Sa*PlsY with $IC_{50}$ values of 9.7 μM and 22.1 μM, respectively (**Fig. 1b**). It also inhibited PlsY orthologs from *Listeria monocytogenes* with $IC_{50}$ values of 49.0 μM (**Fig. 1b**).

### Gpatin competes with the lipid substrate acyl-phosphate (acylP)

To characterize the inhibitory mechanism of Gpatin, we performed enzyme kinetic analyses at varying substrate concentrations. Increasing concentrations of Gpatin had minimal effects on the apparent $K_m$ for glycerol-3-phosphate (G3P), whereas the apparent $K_m$ for acylP increased from 2.5 to 10.5 μM (**Fig. 1c, 1d**). These results indicate that Gpatin competes with the lipid substrate acylP for enzyme binding, which is consistent with our docking results (**Fig. S3**).




e

| Pathogen | MIC (μg mL$^{-1}$) | |
|---|---|---|
| | Gpatin | VAN |
| *S. aureus* RN4220 | 8 | 2 |
| *S. aureus* MRSA | 8 | 2 |
| *S. pneumoniae* | 8 | 1 |
| *S. epidermidis* | 16 | 4 |
| *S. pyogenes* | 16 | 4 |

**Fig. 1 | Biochemical and microbiological characterization of the PlsY inhibitor Gpatin. a** Chemical structure of Gpatin. **b** Inhibition of PlsY from *S. pneumoniae* (*Sp*), *S. aureus* (*Sa*), and *L. monocytogenes* (*Lm*) by Gpatin. $IC_{50}$ values were determined from dose-response curves. **c, d** Lineweaver-Burk plots of *Sp*PlsY at the indicated Gpatin concentrations using acyl-phosphate (acylP) (**c**) or glycerol-3-phosphate (G3P) (**d**) as the variable substrate. **e** Minimum inhibitory concentrations (MICs) of Gpatin against the indicated bacterial pathogens. Vancomycin (VAN) served as a positive control. **f** Growth rescue of *S. aureus* RN4220, MRSA USA300, and *S. pneumoniae* ATCC49619 by supplementation with lysophosphatidic acid (LPA), lysophosphatidylglycerol (LPG), or phosphatidic acid (PA). Data in **b, c, d, f** represent mean ± sd (n = 3).

## Gpatin exhibits cross-species activity against Gram-positive pathogens

We next evaluated the antibacterial activity of Gpatin against clinically relevant bacterial pathogens. Gpatin inhibited growth of *S. aureus* strain RN4220 and *S. pneumoniae* with minimum inhibitory concentrations (MICs) of 8 μg mL$^{-1}$ (**Fig. 1d**). Slightly weaker activity was observed against *Streptococcus pyogenes* and *Staphylococcus epidermidis*, with MIC values of 16 μg mL$^{-1}$. Importantly, Gpatin retained equivalent potency against the methicillin-resistant *S. aureus* (MRSA) strain USA300 (MIC of 8 μg mL$^{-1}$) (**Fig. 1d**).

## Gpatin inhibits phospholipid biosynthesis in bacterial cells through PlsY

To investigate whether Gpatin inhibits bacterial growth through PlsY inhibition *in vivo*, we performed lipid rescue experiments. PlsY catalyzes the formation of lysophosphatidic acid (lysoPA), which is subsequently converted into phosphatidic acid (PA), a central intermediate in phospholipid biosynthesis (**Fig. S1a**). We reasoned that supplementation with the product or downstream lipid intermediates should alleviate growth inhibition caused by Gpatin if PlsY is the cellular target.
Indeed, addition of low concentrations of lysoPA partially rescued Gpatin-mediated growth inhibition in both *S. aureus* and *S. pneumoniae* (**Fig. 1e**). At higher concentrations, however, lysoPA itself impaired bacterial growth, likely because of its detergent-like, and hence membrane-disrupting, properties. Importantly, the control lysolipid lysophosphatidylcholine failed to rescue growth inhibition.

We next tested phosphatidic acid (PA), a downstream phospholipid intermediate that is less membrane-disruptive than lysoPA. PA alone had no detectable effect on bacterial growth, whereas supplementation with PA rescued bacterial growth in the presence of Gpatin in both *S. aureus* and *S. pneumoniae* (**Fig. 1f**). Together, these findings support PlsY as the primary cellular target of Gpatin.

## Structure of the *Sp*PlsY-Gpatin complex

To elucidate the structural basis of PlsY inhibition, we sought to determine the cryo-EM structure of the *Sp*PlsY-Gpatin complex using a fiducial antibody against a membrane proximal external region (MPER) peptide[37,38] fused to the N-terminal of *Sp*PlsY (**Fig. S4a**). The Fab-*Sp*PlsY complex (**Fig. S4b**) retained enzymatic activity and responded similar as the wild-type protein to Gpatin (**Fig. S4c**). The structure of the complex was determined at 2.61-Å resolution with imposed *C*2 symmetry (**Table S2, Fig. S5**). The cryo-EM density map was of sufficient quality to model all transmembrane helices unambiguously, although the TMH4-proceeding helix (α2) was not visible.

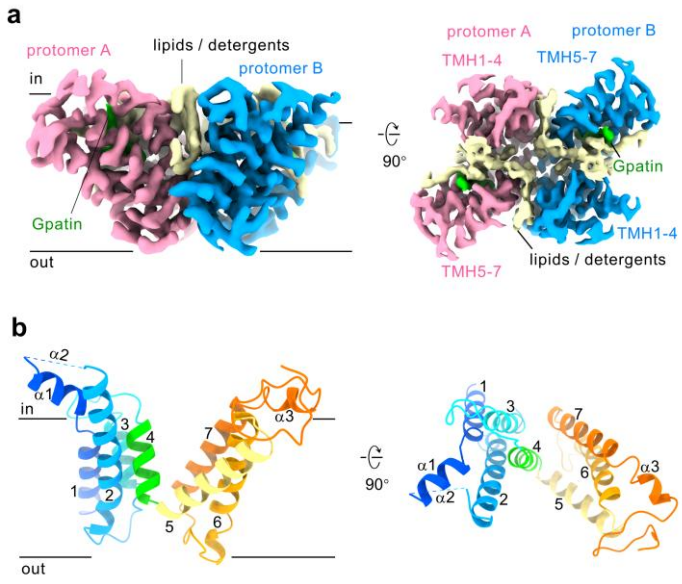



**Fig. 2 | Structure of *Sp*PlsY. a** Side (left) and cytoplasmic (right) views of the cryo-EM density map. Densities corresponding to the MPER peptide and Fab are omitted for clarity. **b** Overall structure of the *Sp*PlsY monomer. Transmembrane helices (TMHs) are numbered, and other α-helices are labeled accordingly. The dashed line denotes the unresolved α2 helix.

*Sp*PlsY forms a V-shaped dimer (**Fig. 2a, Fig. S6**) through intermolecular interactions at the extracellular leaflet and lipid-mediated contacts on the cytosolic side. Each monomer adopts an N-out/C-in seven-transmembrane topology comprising two helical bundles that form a V-shaped architecture (**Fig. 2b**). The OPM-calculated membrane boundary[39] indicates that the protein is almost entirely embedded within the membrane, with essentially no extracellular surface and only limited cytosolic regions exposed to solvent (**Fig. 2b**).

**Molecular basis for Gpatin recognition**

The high-quality cryo-EM density enabled unambiguous modeling of Gpatin (**Fig. 3a**). Gpatin locates in a pocket within the C-terminal transmembrane bundle, engaging the protein through electrostatic, hydrogen-bonding, and hydrophobic interactions (**Fig. 3b**). Its benzoate group extends along TMH6, where the carboxylate interacts

with Arg184 and, more weakly, His185. The central hydrazone linker and pyrazolone carbonyl form bifurcated hydrogen bonds with Ser142, whereas the two phenyl rings anchor the inhibitor through extensive hydrophobic contacts; the N-phenyl group inserts into a pocket lined by Ile174 and Leu177, and the C-phenyl ring packs against Phe128 and Phe129, including a parallel-displaced π-stacking interaction with Phe128.

Consistent with the structural observation, mutation of Arg184 substantially weakened Gpatin inhibition, exhibiting an over 2-fold increase in $IC_{50}$ (**Fig. 3c**). Similarly, the F128A mutation increased $IC_{50}$ to 2-fold. Introduction of a bulky leucine residue at Ala145 (A145L), designed to sterically interfere with inhibitor binding, also slightly impaired inhibition (**Fig. 3c**). In addition, the key residues involved in Gpatin-1 binding, including Phe128, Ser142, Ile182, Arg184, and His185, are strictly conserved among the PlsY orthologs from five pathogens that are inhibited by Gpatin, whereas most of the remaining residues within the binding pocket are also highly conserved (**Fig. S7**).

Notably, the docked pose displayed some similarity with the experimentally observed binding mode, except that the diphenyl moiety inserts deeper into the crevice between the N- and C-terminal TM bundles (**Fig. S8**).

**Competitive inhibition coupled to conformational trapping**

Structural superposition showed that Gpatin partially overlaps with the acylP-binding site (**Fig. 3d**), consistent with the biochemical evidence that Gpatin competitively inhibits acylP binding (**Fig. 1d**). Beyond this competitive mechanism, comparison with our previous crystal structures revealed that Gpatin induces a large conformational rearrangement, in which the N-terminal bundle rotates by approximately 30° and shifts outward by ~18 Å relative to the C-terminal bundle (**Fig. 3d, Movie 1**).

**Competitive inhibition coupled to conformational trapping**

Structural superposition with previous crystal structures[36] showed that Gpatin partially overlaps with the acylP-binding site (**Fig. 3d**), consistent with the biochemical evidence that Gpatin competitively inhibits acylP binding (**Fig. 1d**). Beyond this competitive mechanism, comparison with our previous crystal structures revealed that Gpatin induces a large conformational rearrangement, in which the N-terminal bundle rotates by approximately 30° and shifts outward by ~18 Å relative to the C-terminal bundle (**Fig. 3d, Movie 1**).

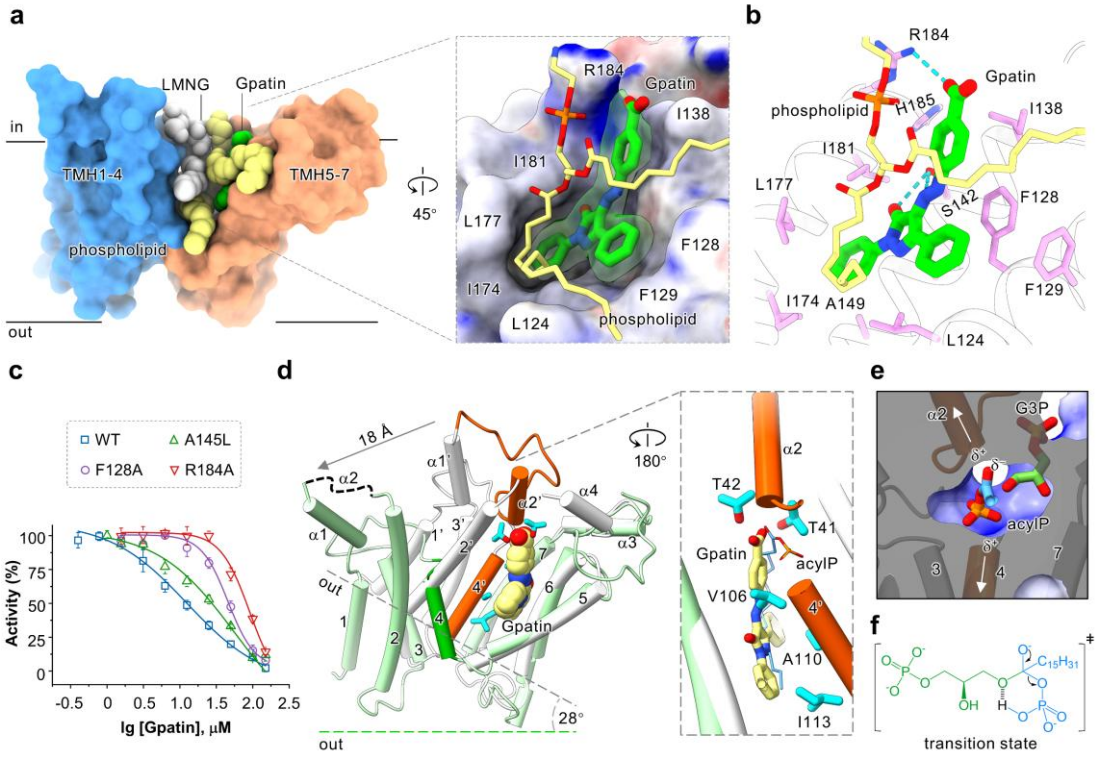



**Fig. 3 | Structural mechanism of PlsY inhibition by Gpatin. a** Overall (left) and expanded (right) views of the Gpatin-binding site. The expanded view depicts the electrostatic surface of *Sp*PlsY together with the bound Gpatin and its corresponding cryo-EM density (semitransparent surface). **b**, Molecular interactions between Gpatin and *Sp*PlsY. Dashed lines indicate hydrogen bonds and salt bridges. **c**, Inhibition of wild-type (WT) and binding-pocket mutants of *Sp*PlsY by Gpatin. **d** Structural superposition of Gpatin-bound *Sp*PlsY (green) and acylP-bound *Aa*PlsY (PDB 5XJ7; grey), aligned using the C-terminal transmembrane-helix (TMH) bundle. Structural elements from the *Aa*PlsY structure are denoted with primes. TMH4 and α2 are

highlighted in red, and residues that sterically clash with Gpatin (yellow) are shown as sticks. AcylP is shown as blue sticks for reference. **e** Formation of the catalytic phosphate hole by TMH4 and α2. **f** Schematic of the transition state during the PlsY catalysis.

Closer examination of the structure revealed that Gpatin disrupts formation of a catalytic competent conformation. The hydrazone moiety sterically clashes with Val106, Ala110, and Ile113 on TMH4, whereas the benzoate group occupies the position of Thr41 and Thr42 at the N-terminal tip of α4 (**Fig. 3d**). In the absence of Gpatin, these two structural elements generate the positively charged "phosphate hole" through their exposed intramembrane helix dipoles (**Fig. 3e**), a feature essential for acylP recognition[36]. In addition, the convergent dipoles are expected to stabilize the negatively charged tetrahedral intermediate (the carbonyl oxyanion) formed during the substrate-assisted acyl-transfer reaction (**Fig. 3e**). By preventing assembly of this catalytic motif, Gpatin traps PlsY in an open, catalytically incompetent conformation.

**Anti-infective efficacy of Gpatin in skin infection model**

To evaluate the *in vivo* efficacy of Gpatin, we first employed a murine model of MRSA skin infection (**Fig. 4a**). Subcutaneous inoculation of the USA300 strain consistently produced well-defined dermonecrotic lesions within 24 h, with no significant differences in lesion size among treatment groups at the onset of therapy (**Fig. S9a**). Vancomycin was included as a positive-control antibiotic to validate the responsiveness of the infection model. Topical administration of Gpatin (25 mg $kg^{-1}$, twice daily for 3 days) significantly suppressed lesion progression compared with vehicle-treated mice (**Fig. 4b**). Gpatin also reduced the bacterial burden within infected lesions (**Fig. 4c**). Histological examination by H&E staining further showed that Gpatin substantially alleviated inflammatory cell infiltration and tissue damage relative to vehicle-treated animals (**Fig. 4d**).

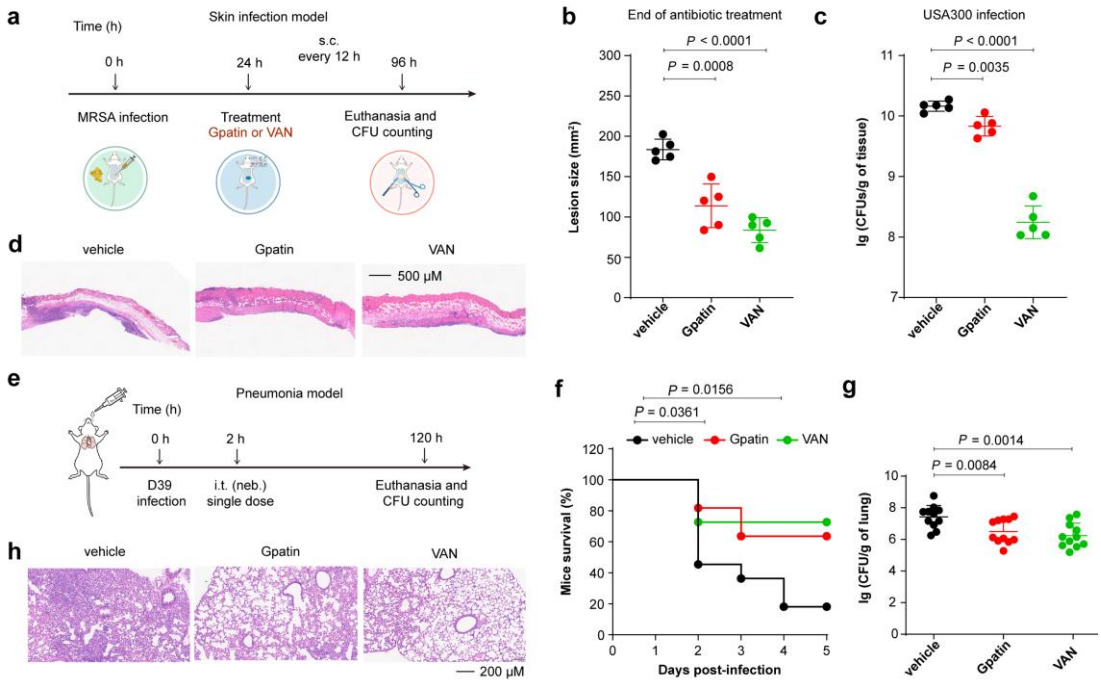



**Fig. 4 | Anti-infective activity of Gpatin in murine infection models. a**, Experimental scheme for the MRSA (USA300) skin infection model. **b**, Representative images and quantification of skin lesion size following treatment with vehicle, Gpatin, or vancomycin (VAN). **c**, Bacterial burdens in infected skin. **d**, Representative H&E-stained sections of infected skin. Scale bar, 500 μm. **e**, Experimental scheme for the *S. pneumoniae* D39 pneumonia model. **f**, Kaplan-Meier survival curves. **g**, Lung bacterial burdens following nebulized treatment. **h**, Representative H&E-stained lung sections. Scale bar, 200 μm. Data represent mean ± sem (**b, c,** n = 5; **g,** n = 11). Statistics methods are included in Methods.

## Anti-infective efficacy of Gpatin in pneumonia model

We next assessed the antibacterial activity of Gpatin in a murine model of *S. pneumoniae* D39 pneumonia (**Fig. 4e**). Given the hydrophobic nature of Gpatin, we first evaluated its activity under protein-rich conditions by testing bacterial growth in the presence of bovine serum albumin (BSA). Gpatin showed no detectable inhibition of *S. pneumoniae* growth even at 32 μg $mL^{-1}$ in the presence of BSA, suggesting reduced effective availability under these conditions. Therefore, Gpatin was administered by intratracheal nebulization (i.t. (neb.)) to maximize drug exposure at the site of infection.

A single nebulized dose of Gpatin (2 mg $kg^{-1}$) significantly prolonged survival and reduced bacterial loads in the lungs of infected mice compared with vehicle-treated controls (**Fig. 4f, 4g; Fig. S9c**), without causing appreciable body-weight loss (**Fig. S9d**). Histological analysis further revealed that Gpatin markedly attenuated pulmonary inflammation and tissue injury relative to the vehicle group, with pathological improvement comparable to that observed in vancomycin-treated control animals (**Fig. 4h**).

Together, these findings demonstrate that Gpatin exhibits anti-infective activity *in vivo* against both MRSA and *S. pneumoniae*, providing pharmacological support for PlsY as a tractable antibacterial target.

## DISCUSSION

The continuing rise of multidrug-resistant bacteria underscores the need for antibacterial agents with fundamentally new mechanisms of action. In this study, we identified Gpatin, a small-molecule inhibitor of the membrane phospholipid acyltransferase PlsY with activity across multiple bacterial species, and characterized its antibacterial activity through biochemical, microbiological, structural, and *in vivo* analyses.

Previous studies demonstrated that PlsY can be inhibited by substrate analogues such as acyl sulfates[34,40], providing proof of principle that the enzyme is chemically tractable. Our work extends this concept by identifying a chemically distinct inhibitor with antibacterial efficacy *in vitro* and *in vivo*, establishing PlsY as a viable target for structure-guided antibiotic discovery.

A notable feature of Gpatin is its unusual inhibitory mechanism in two respects. First, Gpatin induces a substantial conformational rearrangement that disrupts formation of the catalytic phosphate hole, revealing an unexpected vulnerability beyond the

substrate-binding site observed in previous crystal structures[36]. This conformational plasticity expands the chemical space available for PlsY-targeting inhibitors, providing greater scope for scaffold optimization. Second, Gpatin binds within a partially membrane-exposed pocket formed by PlsY and surrounding phospholipids, relying predominantly on hydrophobic interactions. This hybrid protein-lipid binding environment may contribute to activity across different PlsY orthologs, although the hydrophobic binding mode may also present challenges for systemic use. The conformational plasticity of PlsY may permit the introduction of additional polar functionality while preserving binding. For example, the benzoate end of Gpatin may be amenable to the introduction of polar substituents to engage Arg184 and His185 while reducing overall hydrophobicity, potentially improving performance under serum-containing conditions.

Although Gpatin exhibits promising antibacterial activity both in vitro and *in vivo*, its limited serum stability currently restricts its potential for systemic administration. Nevertheless, the efficacy observed in the murine skin infection model highlights the potential of Gpatin or related analogues for topical antibacterial applications.

The broader applicability of PlsY inhibition in Gram-negative bacteria may be constrained by the presence of additional GPAT activities, such as PlsB[41,42], that can compensate for PlsY loss. Thus, co-targeting PlsY and PlsB may provide a strategy to overcome GPAT redundancy. In addition, emerging evidence indicates that the PlsX-PlsY pathway contributes to membrane lipid homeostasis, including coordination of phospholipid and lipopolysaccharide biosynthesis[43]. In *Escherichia coli*, loss of *plsY* is synthetically lethal in a Δ*plsX* background[33], highlighting a genetic dependency that could be leveraged through simultaneous inhibition of PlsX and PlsY.

To our knowledge, Gpatin is the first structurally characterized small-molecule inhibitor of PlsY. By revealing an exploitable inhibitory mechanism and providing a

blueprint for scaffold optimization, our study establishes PlsY as a chemically tractable antibacterial target and provides a framework for future development of PlsY-targeting antibacterial agents.

## REFERENCE


1 Howden, B. P. *et al.* Staphylococcus aureus host interactions and adaptation. *Nature Reviews Microbiology* **21**, 380-395 (2023).

2 Narciso, A. R., Dookie, R., Nannapaneni, P., Normark, S. & Henriques-Normark, B. Streptococcus pneumoniae epidemiology, pathogenesis and control. *Nature Reviews Microbiology* **23**, 256-271 (2025).

3 Naghavi, M. *et al.* Global burden of bacterial antimicrobial resistance 1990–2021: a systematic analysis with forecasts to 2050. *The Lancet* **404**, 1199-1226 (2024).

4 Turner, N. A. *et al.* Methicillin-resistant Staphylococcus aureus: an overview of basic and clinical research. *Nature Reviews Microbiology* **17**, 203-218 (2019).

5 Thacharodi, A. *et al.* Methicillin-resistant Staphylococcus aureus is raising global concern as it overcomes immune challenges through various virulence mechanisms. *iScience* **29**, 114376 (2026).

6 Li, L. *et al.* Epidemiological characteristics and antibiotic resistance mechanisms of Streptococcus pneumoniae: An updated review. *Microbiological Research* **266**, 127221 (2023).

7 Saravolatz, L. D. & Stein, G. E. Plazomicin: A New Aminoglycoside. *Clin Infect Dis* **70**, 704-709 (2020).

8 Bassetti, M. *et al.* Meropenem-Vaborbactam for Treatment of Carbapenem-Resistant Enterobacterales: A Narrative Review of Clinical Practice Evidence. *Infect Dis Ther* **14**, 973-989 (2025).

9 Zhanel, G. G. *et al.* Review of Eravacycline, a Novel Fluorocycline Antibacterial Agent. *Drugs* **76**, 567-588 (2016).

10 Kumar, R., Sohal, J. S., Singh, A. V. & Chauhan, D. S. Pretomanid for the treatment of drug resistant pulmonary tuberculosis: a comprehensive review. *Arch Microbiol* **208**, 35 (2025).

11 Roustaye Gourabi, M. J. *et al.* Cefiderocol: A Comprehensive Review of Chemistry, Mechanisms of Resistance, and Clinical Applications in the Era of Multidrug Resistance. *Curr Microbiol* **83**, 25 (2025).

12 Mi, R. *et al.* Efficacy and safety of contezolid in the treatment of Gram-positive bacterial infections in patients with hematological malignancies: a retrospective study. *European Journal of Clinical Microbiology & Infectious Diseases* **44**, 3047-3055 (2025).

13 Lee, S. H. *et al.* TarO-specific inhibitors of wall teichoic acid biosynthesis restore β-lactam efficacy against methicillin-resistant staphylococci. *Science Translational Medicine* **8**, 329ra332-329ra332 (2016).

14 Srinivas, N. *et al.* Peptidomimetic antibiotics target outer-membrane biogenesis in Pseudomonas aeruginosa. *Science* **327**, 1010-1013 (2010).

15 Pahil, K. S. *et al.* A new antibiotic traps lipopolysaccharide in its intermembrane transporter. *Nature* **625**, 572-577 (2024).

16 Zampaloni, C. *et al.* A novel antibiotic class targeting the lipopolysaccharide transporter. *Nature* **625**, 566-571 (2024).
17 Gerusz, V. *et al.* The bactericidal FabI inhibitor Debio 1453 clears antibiotic-resistant Neisseria gonorrhoeae infection in vivo. *Nature Communications* **16**, 8309 (2025).
18 Kaul, M. *et al.* TXA709, an FtsZ-Targeting Benzamide Prodrug with Improved Pharmacokinetics and Enhanced In Vivo Efficacy against Methicillin-Resistant Staphylococcus aureus. *Antimicrobial Agents and Chemotherapy* **59**, 4845-4855 (2015).
19 Ling, L. L. *et al.* A new antibiotic kills pathogens without detectable resistance. *Nature* **517**, 455-459 (2015).
20 Schneider, T. *et al.* Plectasin, a fungal defensin, targets the bacterial cell wall precursor Lipid II. *Science* **328**, 1168-1172 (2010).
21 Shukla, R. *et al.* An antibiotic from an uncultured bacterium binds to an immutable target. *Cell* **186**, 4059-4073.e4027 (2023).
22 Sati, H. *et al.* The WHO Bacterial Priority Pathogens List 2024: a prioritisation study to guide research, development, and public health strategies against antimicrobial resistance. *The Lancet Infectious Diseases* **25**, 1033-1043 (2025).
23 Esposito, S. *et al.* Recent Changes in the Epidemiology of Group A Streptococcus Infections: Observations and Implications. *Microorganisms* **13** (2025).
24 Song, M., Chen, S., Lin, W. & Zhu, K. Targeting bacterial phospholipids and their synthesis pathways for antibiotic discovery. *Progress in Lipid Research* **96**, 101307 (2024).
25 Carter, A. M., Woods, E. C. & Bogyo, M. Chemical strategies for targeting lipid pathways in bacterial pathogens. *Curr Opin Chem Biol* **86**, 102596 (2025).
26 Lu, K. *et al.* Biological evaluation and chemoproteomics reveal potential antibacterial targets of a cajaninstilbene-acid analogue. *Eur J Med Chem* **188**, 112026 (2020).
27 Radka, C. D. & Rock, C. O. Mining Fatty Acid Biosynthesis for New Antimicrobials. *Annu Rev Microbiol* **76**, 281-304 (2022).
28 Price, A. C. *et al.* Inhibition of beta-ketoacyl-acyl carrier protein synthases by thiolactomycin and cerulenin. Structure and mechanism. *J Biol Chem* **276**, 6551-6559 (2001).
29 Bibens, L., Becker, J. P., Dassonville-Klimpt, A. & Sonnet, P. A Review of Fatty Acid Biosynthesis Enzyme Inhibitors as Promising Antimicrobial Drugs. *Pharmaceuticals (Basel)* **16** (2023).
30 Parsons, J. B. & Rock, C. O. Bacterial lipids: metabolism and membrane homeostasis. *Prog Lipid Res* **52**, 249-276 (2013).
31 Lu, Y. J. *et al.* Acyl-phosphates initiate membrane phospholipid synthesis in Gram-positive pathogens. *Mol Cell* **23**, 765-772 (2006).
32 Lu, Y. J., Zhang, F., Grimes, K. D., Lee, R. E. & Rock, C. O. Topology and active site of PlsY: the bacterial acylphosphate:glycerol-3-phosphate acyltransferase. *J Biol Chem* **282**, 11339-11346 (2007).
33 Yoshimura, M., Oshima, T. & Ogasawara, N. Involvement of the YneS/YgiH and PlsX proteins in phospholipid biosynthesis in both Bacillus subtilis and Escherichia coli. *BMC Microbiol* **7**, 69 (2007).
34 Grimes, K. D. *et al.* Novel acyl phosphate mimics that target PlsY, an essential acyltransferase in gram-positive bacteria. *ChemMedChem* **3**, 1936-1945 (2008).
35 Cherian, P. T. *et al.* Acyl-sulfamates target the essential glycerol-phosphate acyltransferase (PlsY) in

Gram-positive bacteria. *Bioorg Med Chem* **20**, 4985-4994 (2012).
36 Li, Z. *et al.* Structural insights into the committed step of bacterial phospholipid biosynthesis. *Nature Communications* **8**, 1691 (2017).
37 McIlwain, B. C. *et al.* N-terminal Transmembrane-Helix Epitope Tag for X-ray Crystallography and Electron Microscopy of Small Membrane Proteins. *J Mol Biol* **433**, 166909 (2021).
38 Wang, Y. *et al.* Transport and inhibition mechanism for VMAT2-mediated synaptic vesicle loading of monoamines. *Cell Res* **34**, 47-57 (2024).
39 Lomize, M. A., Pogozheva, I. D., Joo, H., Mosberg, H. I. & Lomize, A. L. OPM database and PPM web server: resources for positioning of proteins in membranes. *Nucleic Acids Res* **40**, D370-376 (2012).
40 Cherian, P. T. *et al.* Acyl-sulfamates target the essential glycerol-phosphate acyltransferase (PlsY) in Gram-positive bacteria. *Bioorganic & Medicinal Chemistry* **20**, 4985-4994 (2012).
41 Li, Y., Liu, X., Li, A. & Liu, Z. The phospholipid biosynthesis enzyme PlsB contains three distinct domains for membrane association, lysophosphatidic acid synthesis, and dimerization. *Protein Sci* **35**, e70685 (2026).
42 Zhang, Y. M. & Rock, C. O. Thematic review series: Glycerolipids. Acyltransferases in bacterial glycerophospholipid synthesis. *J Lipid Res* **49**, 1867-1874 (2008).
43 Rex, A. N., Simpson, B. W., Bokinsky, G. & Trent, M. S. PlsX and PlsY: Additional roles beyond glycerophospholipid synthesis in Gram-negative bacteria. *mBio* **15**, e02969-02924 (2024).
44 Maestro, Schrödinger, LLC, (New York, 2017).
45 Prime, Schrödinger, LLC, (New York, NY, 2017).
46 Protein Preparation Wizard workflow, Schrödinger, LLC, (New York, NY, 2017).
47 Epik, Schrödinger, LLC, (New York, NY, , 2017).
48 LigPrep, Schrödinger, LLC, (New York, NY, , 2017).
49 Glide, Schrödinger, LLC, (New York, NY, , 2017).
50 Tang, Y. & Li, D. Developing a High-Throughput Assay for the Integral Membrane Glycerol 3-Phosphate Acyltransferase. *Assay Drug Dev Technol* **17**, 267-274 (2019).
51 Emsley, P., Lohkamp, B., Scott, W. G. & Cowtan, K. Features and development of Coot. *Acta Crystallogr D Biol Crystallogr* **66**, 486-501 (2010).
52 Adams, P. D. *et al.* PHENIX: a comprehensive Python-based system for macromolecular structure solution. *Acta Crystallogr D Biol Crystallogr* **66**, 213-221 (2010).
53 Meng, E. C. *et al.* UCSF ChimeraX: Tools for structure building and analysis. *Protein Sci* **32**, e4792 (2023).

## METHODS

### Virtual Screening

Structure-based virtual screening was performed using the Schrödinger software suite (version 2017-3). Homology models of *Streptococcus pneumoniae* PlsY were generated with the Advanced Homology Modeling workflow[44,45], using the *Aquifex aeolicus* PlsY structures bound to glycerol 3-phosphate (G3P; PDB: 5XJ6) and acyl-phosphate (acylP; PDB: 5XJ7)[36] as templates. The resulting models were prepared using the Protein Preparation Wizard [45-47].

The ChemDiv Stock Library (~1.6 million compounds) [https://www.chemdiv.com/catalog/complete-list-of-compounds-libraries/] was prepared with LigPrep[45,47,48]. Molecular docking was carried out using Glide[49] in a three-stage hierarchical workflow: high-throughput virtual screening (HTVS), standard-precision (SP), and extra-precision (XP). The top 50,000 compounds from each model were retained after HTVS, followed by the top 20,000 after SP docking and the top 5,000 after XP docking.

Candidate compounds were manually selected based on key interactions in their predicted binding modes. Selected compounds were required to satisfy (1) formed polar interactions with residues in the core substrate-binding site and (2) established π-π stacking or extensive hydrophobic interactions within the lipid-binding pocket. To maximize chemical diversity, no more than five compounds sharing the same core scaffold were selected for experimental evaluation.

Additional analogs were also selected from the top 5,000 after XP docking. Selected compounds were required to satisfy two more criteria (1) containing benzoic acid group and (2) having branched aromatic framework. No numerical limit was imposed for compounds sharing the same core scaffold.

### Molecular Cloning

DNA fragments encoding PlsY from *Streptococcus pneumoniae* (*Sp*PlsY, UniProt

P0A4Q0), *Staphylococcus aureus* MRSA252 (*Sa*PlsY, UniProt Q6GH52), and *Listeria monocytogenes* (*Lm*PlsY, UniProt C1L2J2) were codon optimized for *Escherichia coli* expression, synthesized by Azenta (Shanghai, China), and flanked by *BamH*I and *Kpn*I restriction sites. Following digestion with *BamH*I and *Kpn*I, the inserts were ligated into the similarly digested pETSG vector, which encodes a C-terminal thermostable green fluorescent protein (TGP), using T4 DNA ligase. For MPER fusion of *Sp*PlsY, DNA fragments encoding the insertion peptides (**Fig. S5a**) were introduced to pETSG-*Sp*PlsY by PCR. Mutations were made using PCR-based site-directed mutagenesis. All constructs were verified by Sanger sequencing.

**Expression and purification of PlsY proteins**

*Escherichia coli* BL21 (DE3) cells harboring the PlsY expression plasmids were grown overnight in 10 mL Luria-Bertani (LB) medium supplemented with kanamycin (50 μg $mL^{-1}$) at 37 °C. The overnight culture was inoculated (1:100) into M9 medium containing kanamycin and grown at 37 °C with shaking at 200 rpm to an $OD_{600}$ of 0.6–0.8. Cultures were then cooled to 20 °C and protein expression was induced with 0.1 mM IPTG for 22 h.

All purification steps were performed at 4 °C. Cell pellets were resuspended in lysis buffer (150 mM NaCl, 0.1 mM EDTA, 1 mM PMSF, 8 mM $MgCl_2$, 10 μg $m^{-1}$ DNase I, 50 mM Tris-HCl, pH 8.0) and lysed using a high-pressure cell disruptor (Model UH-06, Union, Shanghai, China; flow rate, 100 mL $min^{-1}$) at 600 bar for three passes. Cell debris was removed by centrifugation at 20,000 × g for 30 min. Membranes were collected by centrifugation at 60,000 × g for 1.5 h. Pellets were resuspended in storage buffer (150 mM NaCl, 40% (v/v) glycerol, 1 mM PMSF, and 50 mM Tris-HCl, pH 8.0), flash-frozen in liquid nitrogen, and stored at -80 °C until use.

For cryo-EM studies, membranes prepared from 3 L of E. coli culture expressing pETSG-$PlsY^{EM}$ were thawed and diluted fourfold with buffer containing 150 mM NaCl, 1 mM PMSF, and 50 mM Tris-HCl (pH 8.0). *n*-Dodecyl-β-D-maltopyranoside

(DDM) was added to a final concentration of 1% (w/v), and the suspension was gently stirred for 2 h to solubilize membrane proteins. Insoluble material was removed by centrifugation at 48,000 × g for 1 h, and the supernatant was incubated with 2 mL Strep-Tactin resin pre-equilibrated with Buffer A (150 mM NaCl, 0.2 mM TCEP, and 50 mM Tris-HCl, pH 8.0) for 1.5 h with gentle mixing. The resin was transferred to a gravity-flow column and washed sequentially with three column volumes (CVs) of Buffer A containing 0.02% DDM and 0.01% lauryl maltose neopentyl glycol (LMNG), 0.01% DDM and 0.02% LMNG, 0.2% LMNG (10-min incubation), 0.01% LMNG, and finally 0.005% LMNG. $PlsY^{EM}$ was eluted with Buffer A containing 0.005% LMNG and 5 mM D-desthiobiotin.

For enzymatic studies, membranes prepared from 0.3 L of cell culture were purified using the same procedure, except that 0.2 mL of Strep-Tactin resin was used.

**Expression and purification of Fab 10E8v4**

DNA fragments encoding the light chain and heavy chain of Fab 10E8v4, with a C-terminal hexahistidine tag on the heavy chain, were cloned separately into the pDEC vector containing an N-terminal signal peptide (MDWTWRVFCLLAVAPGAHSD) for transient expression in Expi293F cells. Cells (1 L) were co-transfected with 1 mg of each plasmid using polyethyleneimine (PEI). Valproic acid (VPA) was added to a final concentration of 5 mM, and the cultures were incubated at 37 °C with 5% $CO_2$ and shaking at 125 rpm for 72 h. Culture medium containing the secreted Fab was collected by centrifugation at 1,500 × *g* for 10 min and filtered through a 0.45-μm membrane. The clarified supernatant was adjusted to 150 mM NaCl, 5 mM imidazole, and 50 mM Tris-HCl (pH 8.0), and incubated with Ni-Sepharose resin (Cat. 17531802, GE Healthcare) for 2 h with gentle stirring. The resin was transferred to a gravity-flow column, washed with 20 column volumes (CVs) of wash buffer (150 mM NaCl and 20 mM Tris-HCl, pH 8.0), and the bound Fab was eluted with wash buffer supplemented with 300 mM imidazole. Peak fractions were pooled, adjusted to

10% (v/v) glycerol, flash-frozen in liquid nitrogen, and stored at -80 °C.

**Purification of the PlsY$^{EM}$-Fab complex**

Purified PlsY$^{EM}$ was mixed with Fab 10E8v4 at a 1:1.5 molar ratio (PlsY:Fab). Gpatin was added from a 50 mM DMSO stock to a final concentration of 0.2 mM, and the mixture was incubated for 30 min before loading onto a Superose 6 Increase 10/300 column (Cat. 29091596, Cytiva, Marlborough, MA, USA) equilibrated with SEC buffer containing 0.005% (w/v) LMNG, 150 mM NaCl, 0.2 mM TCEP, and 20 mM Tris-HCl (pH 8.0).

To maintain inhibitor occupancy during sample concentration, a separate aqueous Gpatin stock was prepared by dissolving Gpatin in 1 N NaOH to 100 mM, followed by dilution to 0.5 mM with SEC buffer. Peak fractions were pooled, concentrated to approximately 0.4 mL, and supplemented with the aqueous Gpatin stock to restore a final inhibitor concentration of 0.2 mM. The sample was then concentrated to 3 mg mL$^{-1}$ for cryo-EM grid preparation. Protein concentration was determined from calibrated TGP fluorescence using diluted samples to minimize interference from the UV-visible absorbance of Gpatin.

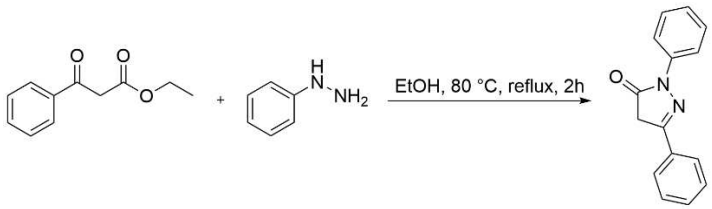
**Fluorescence-detection size-exclusion chromatography (FSEC)**

Purified *Sp*PlsY or MPER-*Sp*PlsY mixed with Fab at the indicated molar ratios was centrifuged at 21,000 × *g* for 30 min at 4 °C before FSEC analysis. Samples were analyzed on an Agilent AdvanceBio SEC 300 Å column (4.6 × 300 mm) connected to a Shimadzu HPLC system equipped with an RF-20A fluorescence detector. The running buffer contained 0.005% (w/v) LMNG, 0.2 mM TCEP, 150 mM NaCl, and 20 mM Tris-HCl (pH 8.0), and the flow rate was 0.3 mL min$^{-1}$. Fluorescence was monitored with excitation and emission wavelengths of 482 and 508 nm, respectively.

**Synthesis of Gpatin**

All solvents and reagents were obtained from commercial suppliers and used without

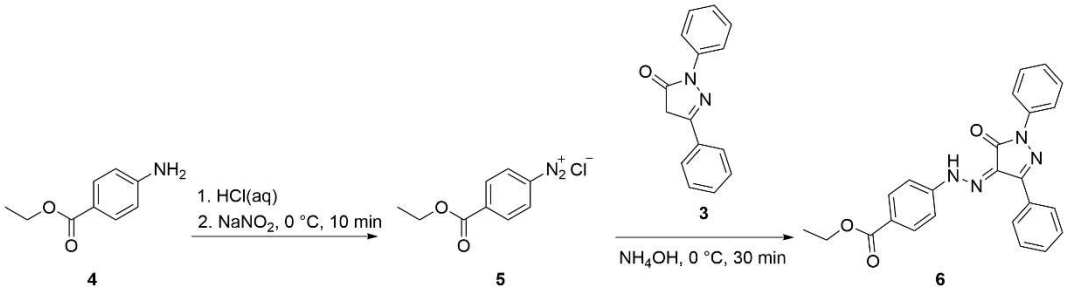
591 further purification. Reactions progress and compound analysis were monitored by
592 HPLC-MS using an Agilent 1200 system coupled to a 6110 mass spectrometry
593 equipped with an Xbridge C18 column (3.5 μm, 4.6 × 50 mm). The HPLC gradient
594 was 5% to 95% acetonitrile in water containing 0.01% formic acid over 6 minutes at a
595 flow rate of 1.0 mL $min^{-1}$. $^{1}H$ NMR and $^{13}C$ NMR spectra were recorded on Bruker
596 400 MHz and 500 MHz spectrometers, respectively, using DMSO-*d6* as solvent.
597 Chemical shifts are reported in parts per million (ppm), and coupling constants are
598 reported in in hertz (Hz). High-resolution mass spectra (HRMS) were obtained using
599 an Agilent G6520 Q-TOF mass spectrometer under electrospray ionization. The purity
600 of Gpatin was determined by analytical HPLC monitored by absorbance at 254 nm.
601
602 *2,5-diphenyl-2,4-dihydro-3H-pyrazol-3-one* (**3**)




603 **1** **2** **3**

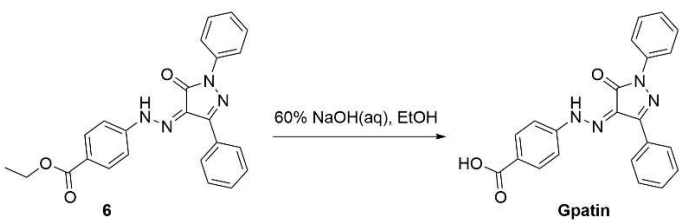
604 Phenylhydrazine **2** (6.2 g, 57.0 mmol, 1.1 eq, 5.6 mL) was dissolved in ethanol (100
605 mL) and stirred at RT (RT, 20 °C). Ethyl benzoylacetate **1** (10.0 g, 52.0 mmol, 1.0 eq)
606 was added, and the mixture was heated under reflux for 2 h. The reaction mixture was
607 cooled to RT, and the solvent was removed under reduced pressure. The residue was
608 suspended in petroleum ether (PE) and stirred for 6h. The suspension was filtered, and
609 the solid was dried to yield compound **3** as a yellow solid (10.9 g, 88.4% yield). $^{1}H$
610 NMR (400 MHz, DMSO-*d6*) δ 11.81 (s, 1H), 7.82 (d, $J$ = 5.9 Hz, 4H), 7.47 (d, $J$ = 6.9
611 Hz, 2H), 7.41 (s, 2H), 7.31 (dd, $J$ = 15.8, 5.7 Hz, 2H), 6.02 (s, 1H). $^{13}C$ NMR (126
612 MHz, DMSO-*d6*) δ 154.8, 150.6, 139.9, 134.4, 130.0, 129.69, 128.9, 127.29, 126.7,
613 126.1, 122.2, 119.4, 86.1.LC-MS $[M + H]^{+}$: 236.5.
614
615

*Ethyl (Z)-4-(2-(5-oxo-1,3-diphenyl-1,5-dihydro-4H-pyrazol-4-ylidene)hydrazineyl)benzoate* (**6**)




Ethyl 4-aminobenzoate 4 (7.7 g, 46.6 mmol, 1.1 equiv.) was dissolved in 4.0 M HCl (31.0 mL), and an aqueous sodium nitrite solution (2.2 M, 32.0 mL, 1.7 equiv.) was added at 0 °C. The mixture was stirred for 10 min at 0 °C. A solution of compound 3 (10.0 g, 42.3 mmol) in tetrahydrofuran (THF, 0.5 M) was then added dropwise together with 1.3 M NH4OH (60.5 mL). The reaction mixture was stirred for 0.5 h at 0 °C, and the resulting precipitate was collected by filtration. The solid was washed with water and dried, followed by slurry purification in EtOAc/$CH_2Cl_2$/petroleum ether (1:1:8, 200 mL) for 3 h at room temperature. The suspension was filtered to afford compound 6 as an orange solid (11.4 g, 65.1% yield). $^1$H NMR (400 MHz, DMSO-*d6*) δ 13.66 (s, 1H), 8.18 (s, 2H), 8.04 (d, *J* = 9.7 Hz, 4H), 7.76 (d, *J* = 7.8 Hz, 2H), 7.54 (d, *J* = 16.5 Hz, 5H), 7.29 (s, 1H), 4.31 (s, 2H), 1.33 (s, 4H). $^{13}$C NMR (126 MHz, DMSO-*d6*) δ 166.1, 157.7, 147.2, 146.2, 138.7, 132.0, 131.2, 130.8, 130.2, 130.0, 129.9, 129.6, 129.4, 128.6, 128.3, 127.5, 126.5, 119.7, 119.3, 117.3, 61.8, 15.2.LC-MS $[M + H]^+$: 412.2; HRMS $[M + H]^+$ (ESI - TOF) calcd for $C_{24}H_{21}N_4O_3$ 413.1608, found 413.1606.

*(Z)-4-(2-(5-oxo-1,3-diphenyl-1,5-dihydro-4H-pyrazol-4-ylidene)hydrazineyl)benzoic acid* (**Gpatin**)



Compound 6 (11.3 g, 27.5 mmol) was dissolved in ethanol (80 mL), followed by addition of 60% (w/w) aqueous NaOH solution (18.4 mL). The mixture was stirred at room temperature for 6 h. After removal of solvent under reduced pressure, the residue was neutralized with 60% (w/w) HCl solution (23 mL), resulting in precipitation of an orange solid. The solid was collected by filtration, washed with PE/ethyl acetate (8:1), and dried to afford Gpatin as an orange powder (9.4 g, 88.4% yield). $^{1}$H NMR (400 MHz, DMSO-*d6*) δ 13.66 (s, 1H), 12.96 (s, 1H), 8.18 (d, *J* = 4.8 Hz, 2H), 8.02 (s, 4H), 7.72 (d, *J* = 6.8 Hz, 2H), 7.54 (dd, *J* = 17.8, 5.9 Hz, 5H), 7.29 (s, 1H). $^{13}$C NMR (126 MHz, DMSO-*d6*) δ 167.7, 157.8, 147.2, 145.8, 138.7, 132.1, 131.1, 130.8, 130.2, 129.9, 129.2, 128.6, 128.3, 126.6, 119.3, 117.2.LC-MS $[M + H]^+$: 384.1; HRMS $[M + H]^+$ (ESI - TOF) calcd for $C_{22}H_{17}N_4O_3$ 385.1295, found 385.1298. Purity: 98.75% by HPLC at 254 nm.

**Enzymatic assay**

PlsY activity was quantified by monitoring inorganic phosphate (Pi) release using *N*-[2-(1-maleimidyl)ethyl]-7-(diethylamino)coumarin-3-carboxamide-labeled phosphate-binding protein (MDCC-PBP) as a fluorescent Pi biosensor[50]. Acyl-phosphate was chemically synthesized from a previous study[36]. Assays were performed in pre-warmed 96-well half-area plates (Cat. 3880, Corning) at 26 °C. Reaction mixtures contained 150 mM NaCl, 0.03% (w/v) LMNG, 100 mM Tris-HCl (pH 8.5), purified PlsY, acyl-phosphate (acylP), and 6 μM MDCC-PBP. Reactions were initiated by addition of glycerol 3-phosphate (G3P), and fluorescence (excitation/emission, 425/466 nm) was recorded every 30 s for 40 min using a SpectraMax M2e plate reader (Molecular Devices, San Jose, CA, USA). Pi production was quantified using a calibration curve generated with known phosphate concentrations.

Protein concentrations were optimized for each PlsY ortholog according to their catalytic activities: *Sp*PlsY, 20 ng mL$^{-1}$; *Sa*PlsY, 8 μg mL$^{-1}$; *Lm*PlsY, 20 ng mL$^{-1}$; and *Sp*PlsY mutants, 40 ng mL$^{-1}$.

For determination of the acylP $K_m$, G3P was fixed at 20 mM, whereas acylP was varied at 2.5, 5, 10, 20, and 40 μM in the presence of 0, 5, 15, or 30 μM Gpatin. For determination of the G3P $K_m$, acylP was fixed at 10 μM, whereas G3P was varied at 2, 4, 8, 16, and 32 mM. Unless otherwise indicated, other assays were performed with 2 mM G3P and 2.5 μM acylP. For inhibition assays, Gpatin was added at the indicated concentrations. The intial inhibitor screening was performed with compounds at 20 μM, whereas $IC_{50}$ measurements were carried out using Gpatin concentrations of 0, 0.4, 0.8, 1.6, 3.2, 6.4, 12.5, 25, 50, 100, and 150 μM. Kinetic parameters were determined using GraphPad Prism v10.1.2.

**Minimum inhibitory concentration (MIC) assay**

Overnight cultures of bacterial strains (*Staphylococcus aureus* RN4220, *S. aureus* USA300, *Streptococcus pneumoniae* ATCC 49619, *Staphylococcus epidermidis* ATCC 1457, and *Streptococcus pyogenes* ATCC 12344) were grown in tryptic soy broth (TSB) at 37 °C with shaking at 220 rpm to an $OD_{600}$ of 0.4-0.6. Cultures were diluted with fresh TSB to an $OD_{600}$ of 0.002. Aliquots (50 μL) were mixed with an equal volume of serially diluted compounds in 96-well plates and incubated statically at 37 °C for 18 h. 3-(4,5-Dimethylthiazol-2-yl)-2,5-diphenyltetrazolium bromide (MTT) solution (10 μL, 5 mg $mL^{-1}$) was then added, followed by incubation for 30 min at 37 °C in the dark. Absorbance at 595 nm was measured using a microplate reader.

**Lipid complementation assay**

Lipid complementation assays were performed as described for the MIC assay, except that Gpatin was fixed at 8 μg $mL^{-1}$ and the indicated lipids (lysophosphatidic acid (lysoPA), lysophosphatidylglycerol (lysoPG), or phosphatidic acid (PA)) were added at concentrations ranging from 0 to 256 μM.

**Mice skin infection model**

Female BALB/c mice (18–20 g) were anesthetized by intraperitoneal injection pentobarbital sodium (70 mg/kg). The dorsal skin was shaved and treated with a depilatory cream 16 h prior to bacterial inoculation. Overnight cultures of *S. aureus* USA300 were diluted 1:500 in tryptic soy broth (TSB) and grown to an optical density at 600 nm ($OD_{600}$) of 1.0. Cells were harvested, washed twice with phosphate-buffered saline (PBS), and resuspended at $4 \times 10^8$ CFU $mL^{-1}$. Each mouse received a subcutaneous injection of 50 μL bacterial suspension ($2 \times 10^7$ CFU) into the dorsal skin. After 24 h post-infection, mice were randomly assigned to treatment groups (n = 5). Lesion areas were calculated using the formula $A = \pi(L/2) \times W/2$ ($A$, area; $L$, length; $W$, width). Gpatin, vancomycin, or vehicle control was prepared in a formulation containing 5% DMSO, 40% PEG 300, 5% Tween-80, and 50% saline, and administered by subcutaneous injection adjacent to the infected site twice daily for 3 days. At the end of the treatment period, mice were sacrificed, and infected skin tissues were collected after separation from underlying fascia and muscle. Tissue samples were homogenized in 1 mL of sterile saline, serially diluted, and plated onto tryptic soy agar (TSA) plates for bacterial enumeration after overnight incubation at 37 °C for. Bacterial burden was expressed as $\log_{10}$ (CFU $g^{-1}$ tissue). For histological analysis, remaining skin samples were fixed in 4% paraformaldehyde, paraffin embedded, sectioned, and stained with hematoxylin and eosin (H&E). Tissue pathology was examined under a light microscope.

**Mice lung infection Model**

Female BALB/c mice (18–20 g, n = 11 mice per group) were anesthetized by intraperitoneal injection of pentobarbital sodium (70 mg $kg^{-1}$). Mice were infected by intranasal instillation of 30 μL *S. pneumoniae* D39 suspension ($1 \times 10^9$ CFU $mL^{-1}$). At 2 h post-infection, mice received a single intratracheally nebulization dose of Gpatin (2 mg $kg^{-1}$), vancomycin (2 mg $kg^{-1}$), or vehicle (5% DMSO, 95% saline) via a micro-nebulizing needle to avoid aspiration risk. Survival and body weight were monitored daily for 5 days. The lungs of mice that died during the experiment and of mice

euthanized at the experimental endpoint were collected and homogenized for CFU enumeration (expressed as $\log_{10}$ CFU $g^{-1}$ tissue). Lungs from three mice per group were fixed in 4% paraformaldehyde, embedded in paraffin, sectioned, and stained with H&E for histological analysis under a light microscope. Statistical analyses were performed in GraphPad Prism 8.0. Survival curves were analyzed using the Mantel-Cox test, and bacterial loads were compared using the two-tailed unpaired Student's *t*-test.

**Cryo-EM sample preparation**

The *Sp*PlsY$^{EM}$-10E8v4 complex (3 µL) was applied onto glow-discharged holey carbon grids (Quantifoil Au R1.2/1.3, 300 mesh) and blotted for 4 s at 8 °C under 100% humidity using a Vitrobot (Thermo Fisher scientific). Grids were plunged into liquid ethane for cryo-cooling.

**Cryo-EM data collection and processing**

Grids were loaded onto a Titan Krios G4 cryo-electron microscope (Thermo Fisher) equipped with a Falcon 4i direct electron device and a Selectris X energy filter. Movie stacks were collected using the EPU software (version 3.8.1 Thermo Fisher) with the Falcon 4i detector operating in counting mode at a total dose of 50 $e^{-}/Å^2$. Data processing was performed using cryoSPARC (v4.7.1) (**Fig. S6**). Micrographs corrected for motion and contrast transfer function (CTF) were used for particle picking (box size 256 pixels, binned by 4). Particles were purified by 2D classification and heterogeneous refinement using *ab initio* models. Particles were then re-extracted (box size 256 pixels) and subjected to multiple rounds of heterogeneous refinement. Particles were recentered to the center of the transmembrane region, re-extracted with a box size of 320 pixels, and polished by reference-based motion correction. The C2-symmetry was applied at the last steps. The final map was obtained through local refinement. Map resolution was estimated using the gold-standard Fourier shell correlation (FSC) criterion of 0.143.

## Model building and refinement

Atomic model was built manually using Coot 0.9.6[51] and refined using Phenix67 1.19.2-4158[52]. Structures were visualized using ChimeraX 1.11[53].

## Animals and Ethics Statement

Female BALB/c mice (18–20 g) were obtained from Zhejiang Vital River Laboratory Animal Technology Co., Ltd. and were housed in the specific pathogen-free facility at the Shanghai Institute of Materia Medica. The animals were kept under a 12 h dark/light cycle with ambient temperature (20–26 °C) and humidity (40–60%). The experimental protocols were approved by the Institutional Animal Care and Use Committee (IACUC) of the Shanghai Institute of Materia Medica (approval number: 2026-01-YCG-13 for *S. aureus* and 2026-05-YCG-15 for *S. pneumoniae*), and all procedures were carried out following relevant ethical guidelines and regulations.

## DATA AVAILABILITY

The coordinates for the models and the cryo-EM maps generated in this study have been deposited in the PDB and EMDB under the accession codes of 43QY and EMD-82078, respectively.

## ACKNOWLEDGEMENT

We thank the staff members of the Center of Cryo-EM of Sun Yat-sen University and of the Shenzhen Medical Academy of Research and Translation (SMART) for technical assistance. This work has been supported by the National Natural Science Foundation of China (W2412096 & 32471246, D.L.; 22494693, C.-G.Y) and the

start-up funds from Sun Yat-sen University.

## AUTHOR CONTRIBUTION

D.L., S.Z. and C.-G.Y. conceived project. Z.Y., H.X., and Y.T. purified protein, characterized enzymes and inhibitors with help from Z.S.. Y.W. performed virtual screening. T.Z. and Y.L. synthesized the compound. T.Z. and Y.P. conducted animal study and carried our animal experiments under supervision of C.-G.Y.. Z.Y. prepared grids. Z.Y. and T.L. collected cryo-EM data. D.L. processed cryo-EM data, oversaw the project, and wrote the manuscript with inputs from Z.Y., Y.W., T.Z., C.-G.Y. and K.K..

## COMPETING INTEREST STATEMENT

D.L., Z.Y., S.Z., and Y.W. are named inventors on a patent application (#2026106446983) related to Gpatin submitted to the Chinese Patent Office by Sun Yat-sen University and ShanghaiTech University.

# Supplementary files

**Supplementary Fig. 1-9**

**Supplementary Table 1-2**

**Still image of Movie and Movie legends**

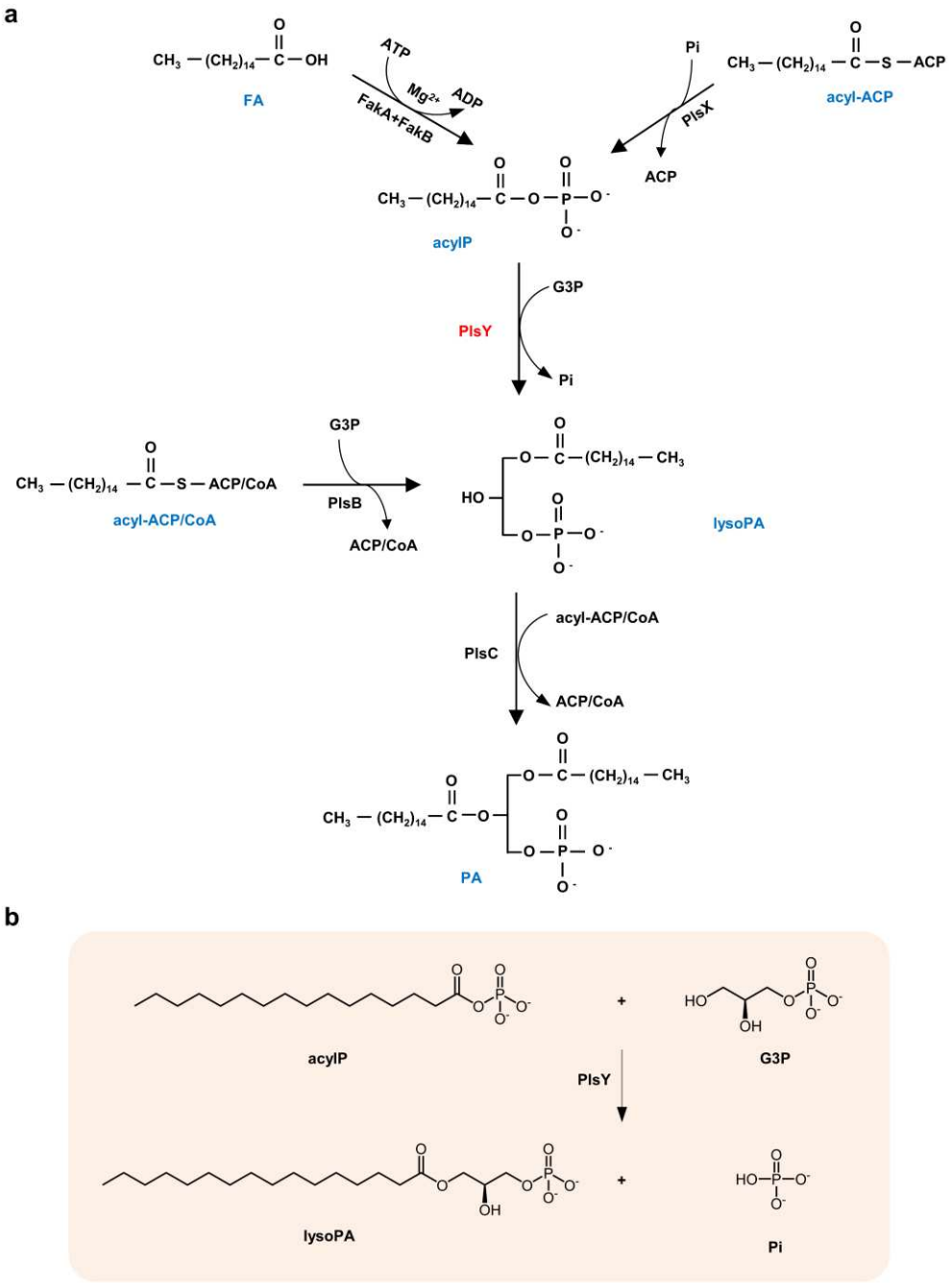



**Fig. S1 | Role of PlsY in bacterial phospholipid biosynthesis. a** Phosphatidic acid (PA) synthesis pathway. ACP, acyl-carrier protein; ADP/ATP, adenosine di/tri-phosphate; CoA, coenzyme A; FA, fatty acid. **b** Enzymatic reaction catalyzed by PlsY. AcylP, acyl-phosphate; G3P, glycerol 3-phosphate; lysoPA, lysophosphatidic acid.

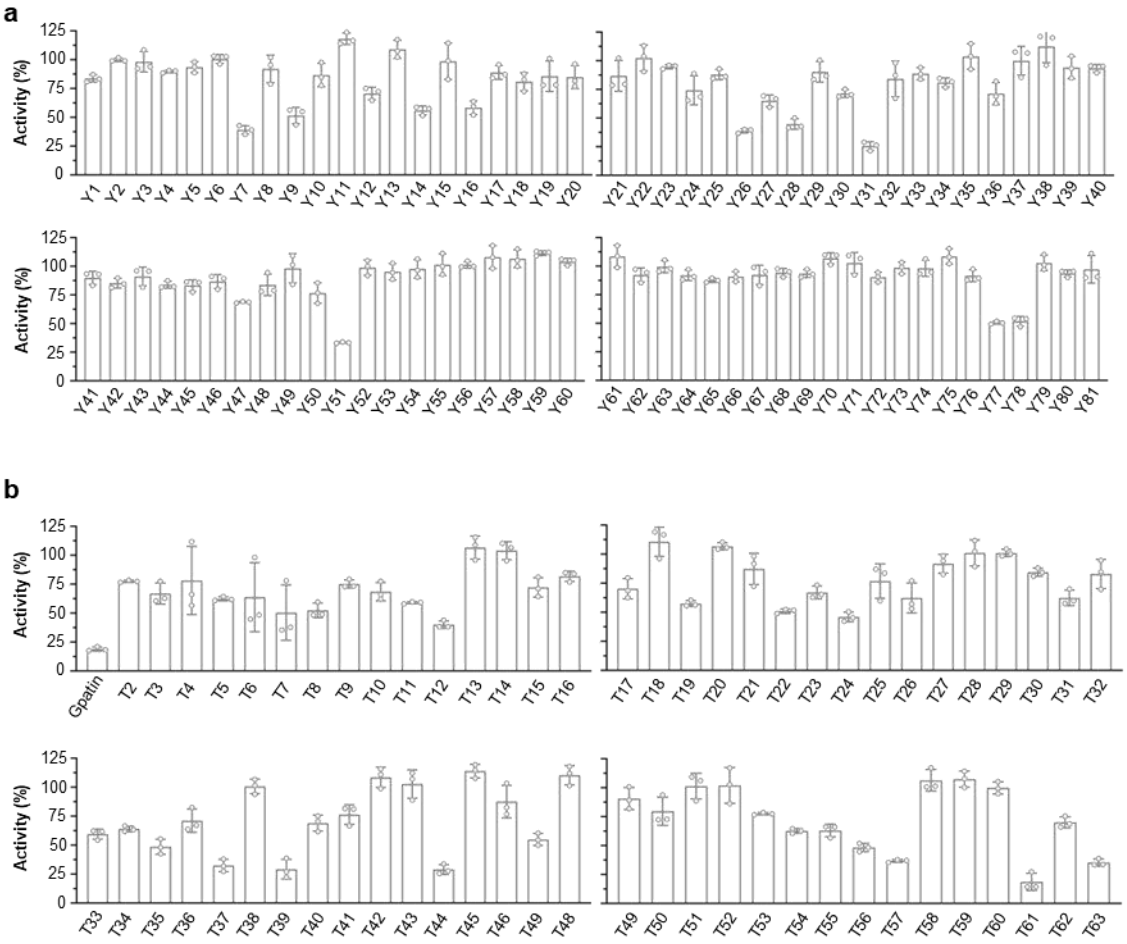



**Fig. S2 | Identification of Gpatin. a** Enzymatic inhibition assay of compounds identified from the initial virtual screening. **b** Enzymatic inhibition assay of chemically related compounds selected based on the results from **a**. Compounds and *Sp*PlsY were used at final concentrations of 20 μM and 20 ng $mL^{-1}$, respectively.

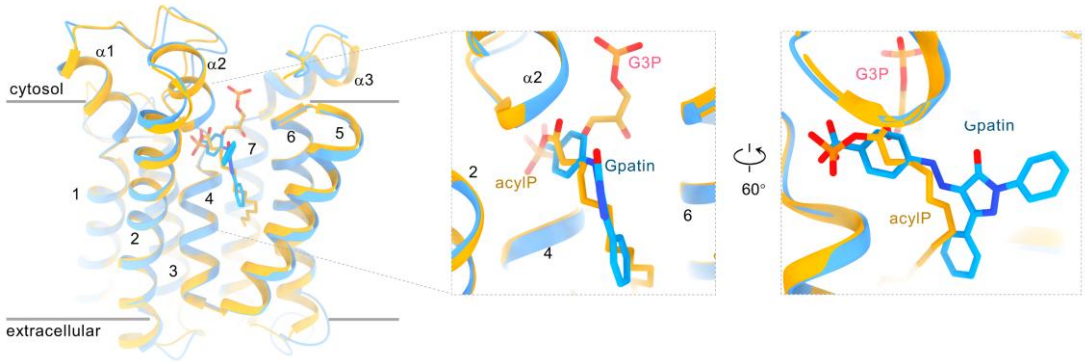



**Fig. S3 | Molecular docking of Gpatin into *Sp*PlsY.** The docked Gpatin-*Sp*PlsY complex (orange) was aligned to the acylP-bound structure (PDB 5XJ7; blue). Protein structures are shown as cartoons. AcylP and G3P (superposed from PDB entry 5XJ6), and Gpatin are shown as sticks.

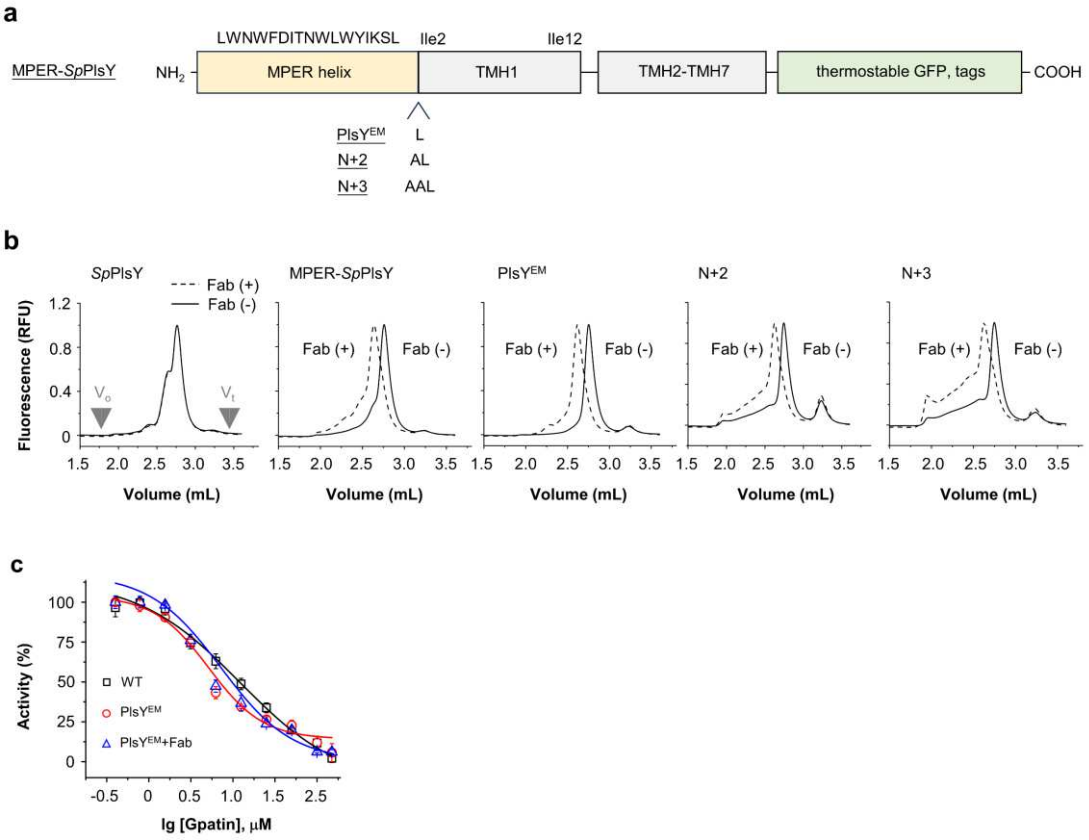
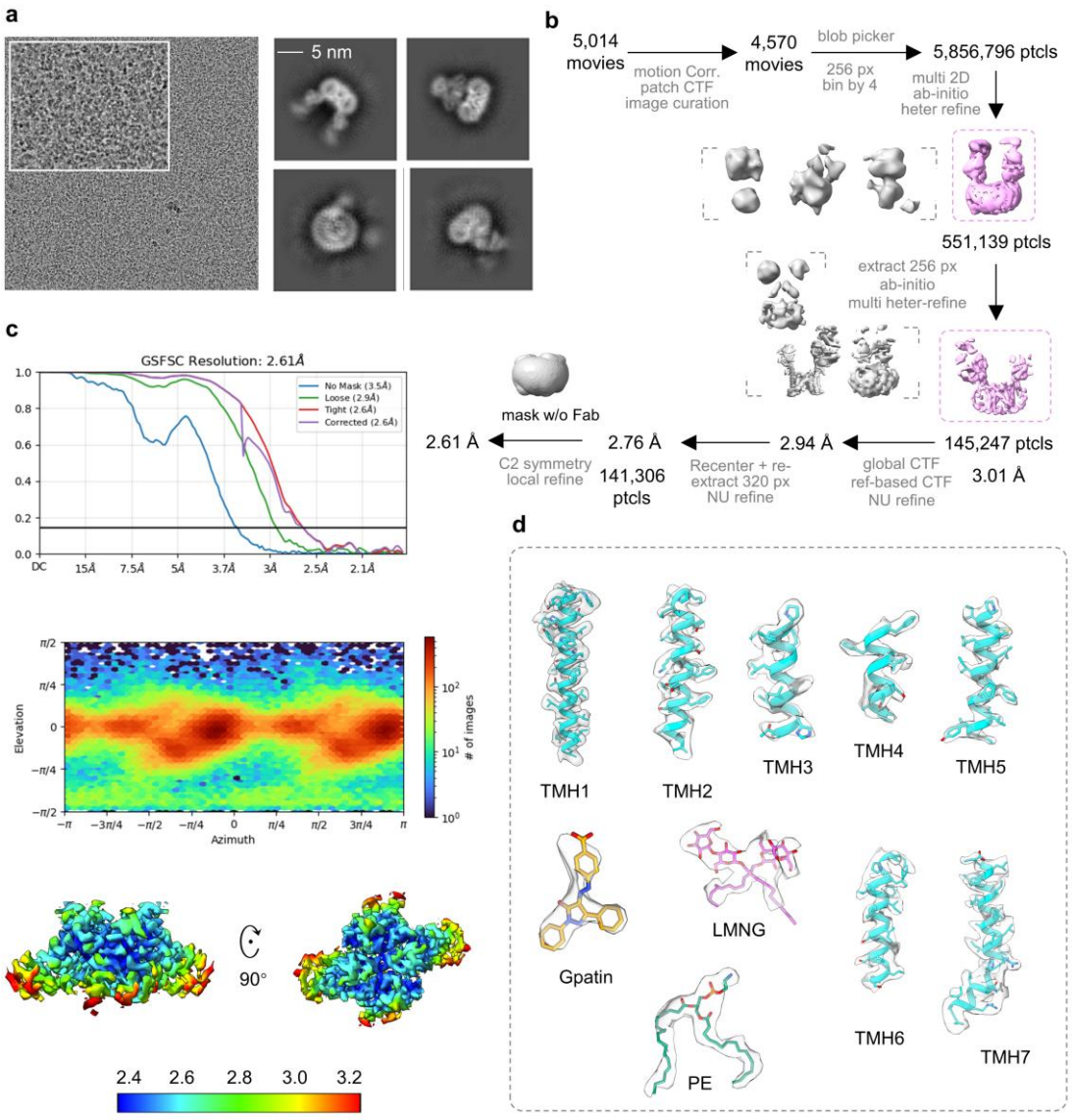
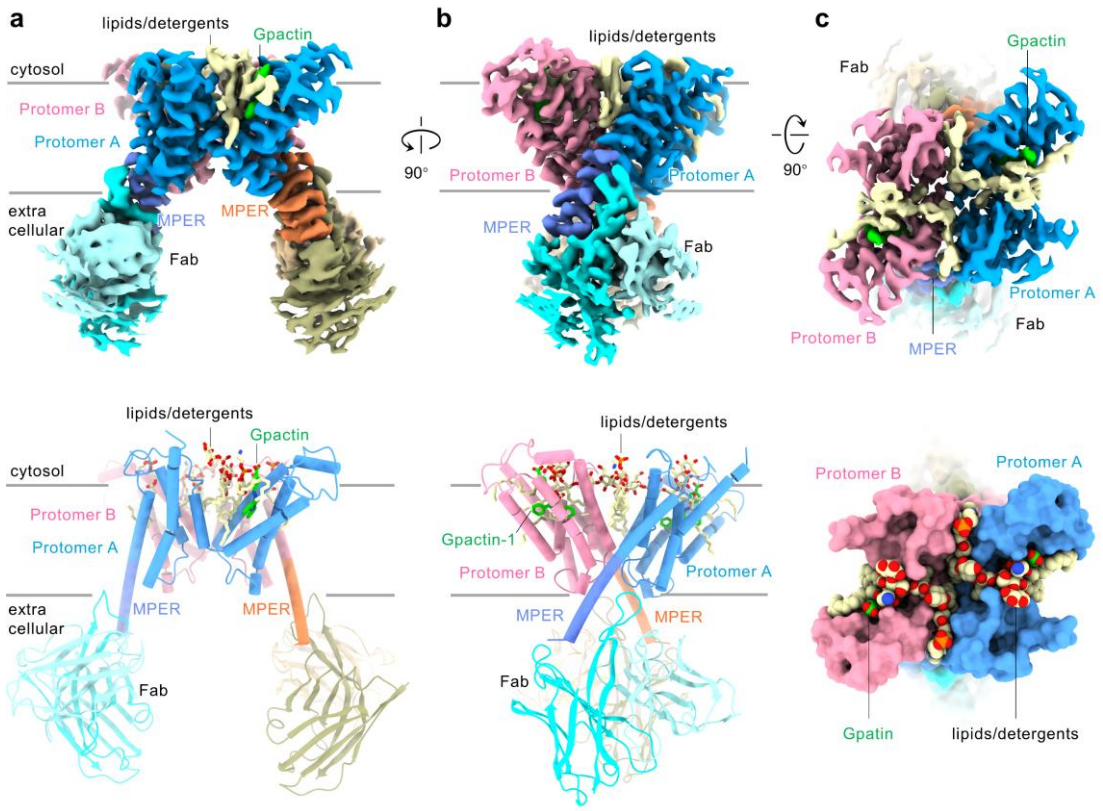



**Fig. S4 | Screening of MPER-fusion constructs. a** Schematic representation of different MPER-*Sp*PlsY fusion constructs. TMH, transmembrane helices. Amino acid sequences are shown using the one-letter code. **b** Fluorescence-detection size exclusion chromatography (FSEC) profile of *Sp*PlsY constructs in the presence (solid lines) or absence (dashed lines) of Fab 10E8v4. $V_0$ and $V_t$ indicate the void volume and total column volume, respectively. **c** Enzymatic activity of the engineered construct ($PlsY^{EM}$) used for cryo-EM in the absence (red) or presence (blue) of the anti-MPER Fab.




827

828 **Fig. S5 | Cryo-EM data processing and representative density features of the**
829 ***Sp*PlsY-Fab complex. a** Representative cryo-EM micrograph and selected 2D class
830 averages. **b** Cryo-EM data processing workflow. **c** Gold-standard Fourier shell
831 correlation (FSC) curves (top), angular distribution plots (middle), and local
832 resolution estimation (bottom; shown for *Sp*PlsY only). **d** Representative cryo-EM
833 densities and fitted models for transmembrane helices, Gpatin, lipids, and detergents.
834 LMNG, lauryl maltose neopentyl glycol; PE, phosphatidylethanolamine; TMH,
835 transmembrane helix.

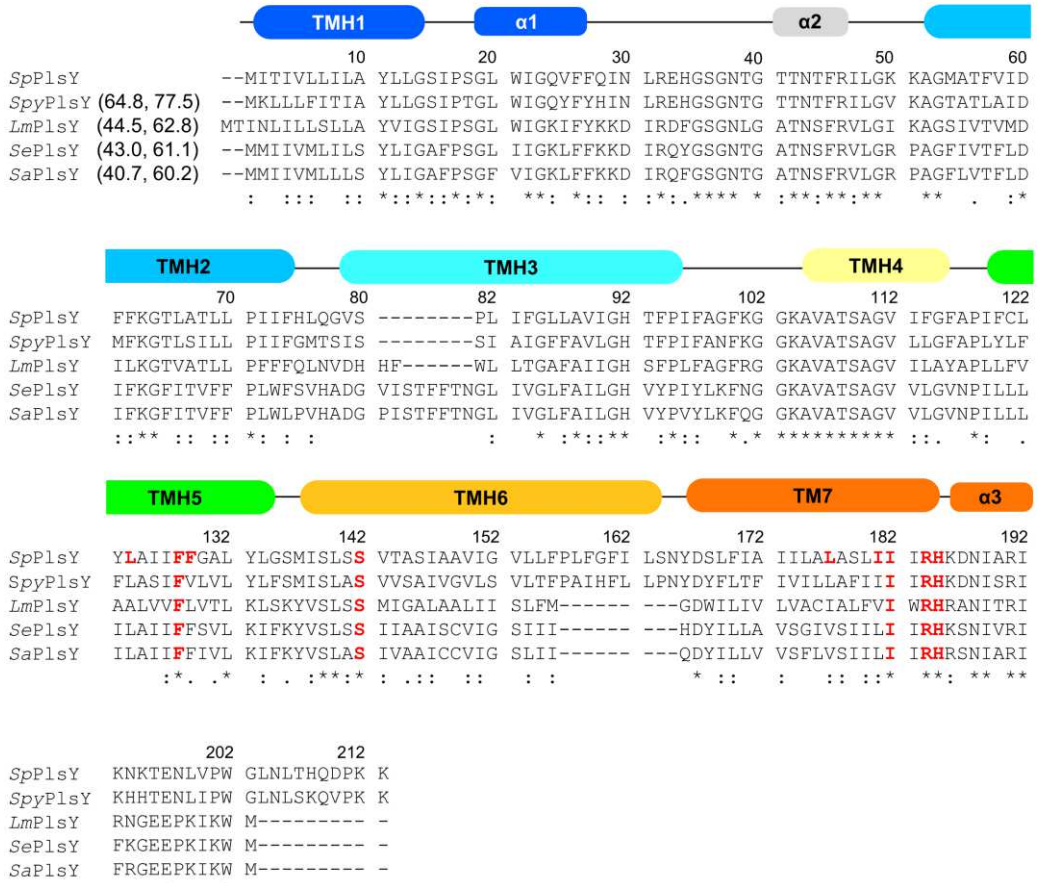



836

837 **Fig. S6 | Cryo-EM density map and structure of the *Sp*PlsY-Fab complex. a-c**

838 Cryo-EM density maps (top) and corresponding structures (bottom) viewed from the

839 indicated orientations.




840

841 **Fig. S7 | Sequence alignment of PlsY orthologs inhibited by Gpatin.** Sequence
842 alignment of PlsY orthologs from *S. pneumoniae* (*Sp*PlsY), *S. pyogenes* (*Spy*PlsY), *L.*
843 *monocytogenes* (*Lm*PlsY), *S. epidermidis* (*Se*PlsY), and *S. aureus* (*Sa*PlsY), was
844 generated using ClustalW. Sequence identity and similarity relative to *Sp*PlsY are
845 indicated in brackets. Asterisks, colons, and dots denote identical, conserved, and
846 semi-conserved residues, respectively. Secondary structure elements are color-coded
847 as in **Fig. 2b**. TM denotes transmembrane helices and α denotes non-transmembrane
848 helices. Residues involved in Gpatin-binding are highlighted in red.

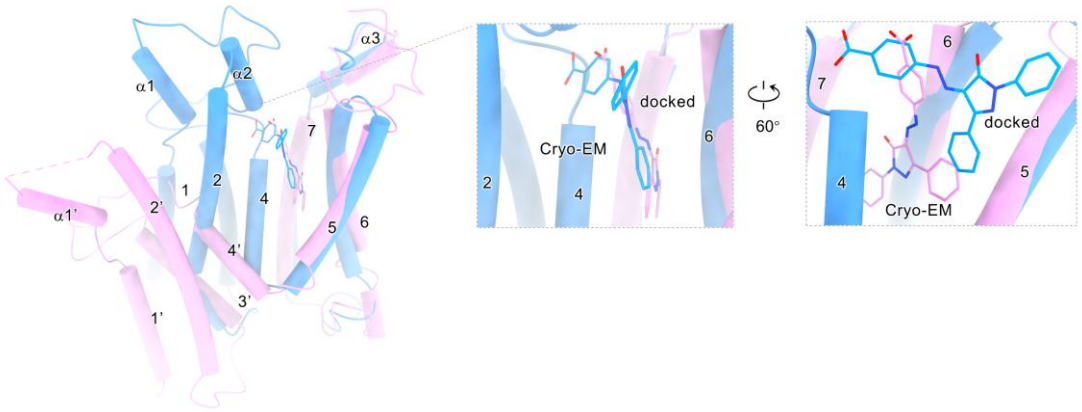



**Fig. S8 | Comparison of the docked and experimentally determined Gpatin-*Sp*PlsY complexes.** The docked structure is shown in blue and the cryo-EM structure in pink. Transmembrane helices are numbered for the docked structure and labeled with prime symbols for the cryo-EM structure. Gpatin is shown as sticks.

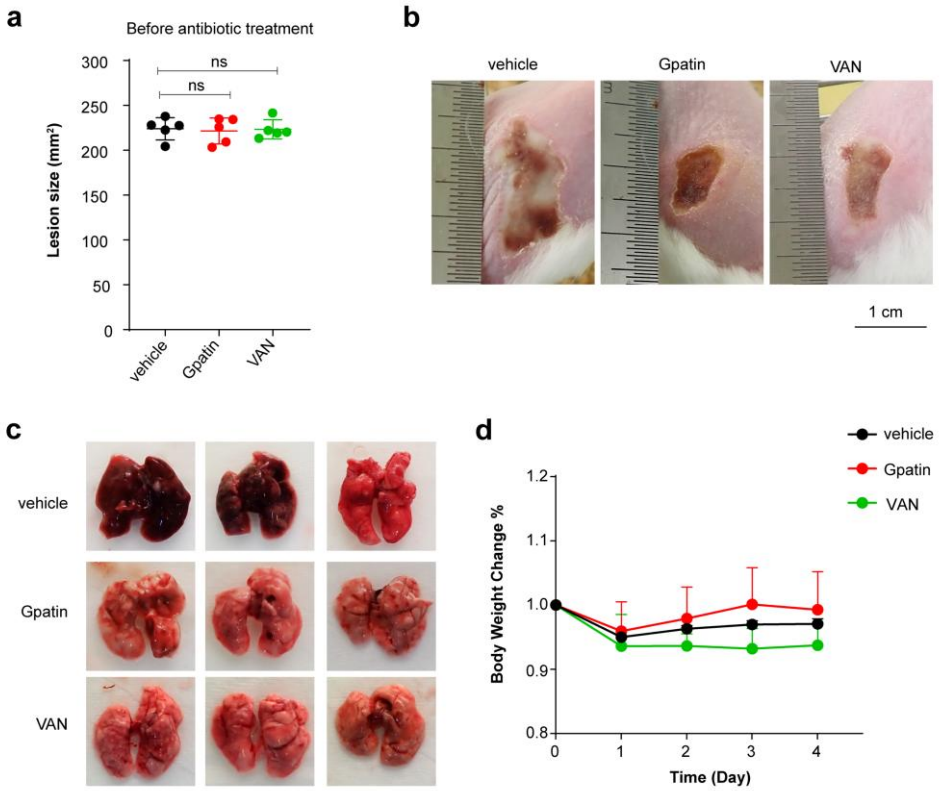
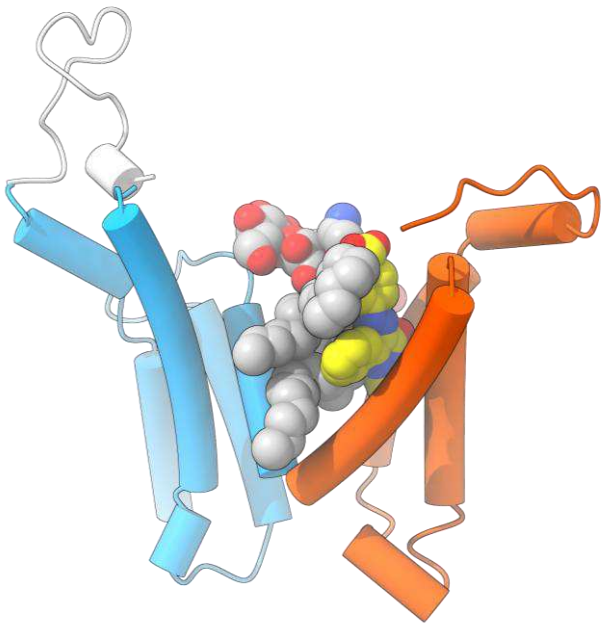
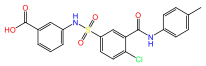
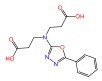
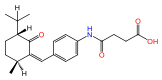
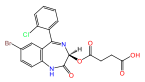
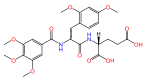
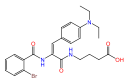
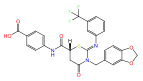
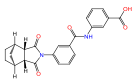
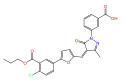
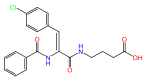
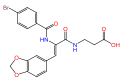
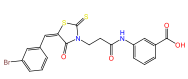
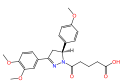
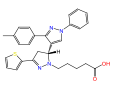
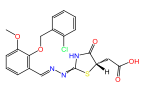


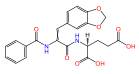
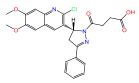
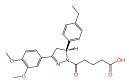
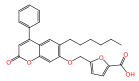
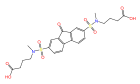
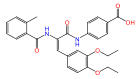
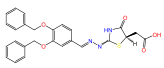
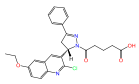
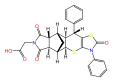
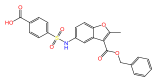
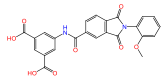
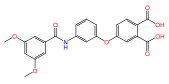
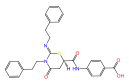
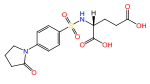

**Fig. S9 | *In vivo* anti-infective activity of Gpatin in skin and lung infection models. a** Necrotic skin lesion size at Day 0 following infection. BALB/c mice (n = 5) were infected with USA300. **b** Representative images of necrotic skin lesions at the endpoint of the experiment. Scale bar, 1 cm. **c** Representative gross images of lungs after 5 days of treatment. **d** Body weight changes of D39 infected mice following a single intratracheal nebulized administration of vancomycin (VAN) or Gpatin over 5 days.

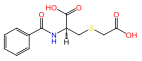
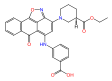
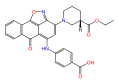
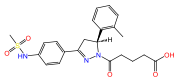
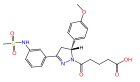
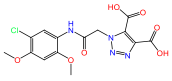
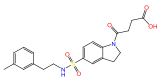
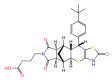
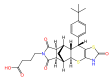
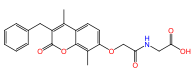
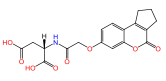
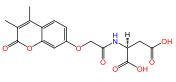


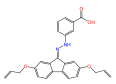
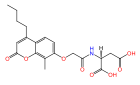
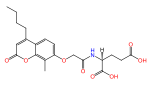
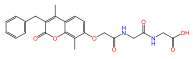
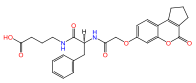
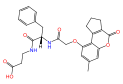
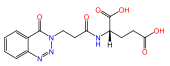
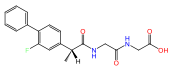
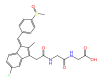
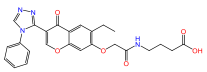
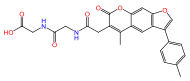
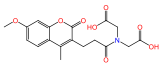
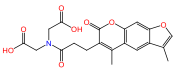
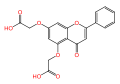
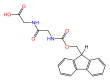
**Movie 1 | Gpatin binding induces a large conformational rearrangement in *Sp*PlsY.** A molecular morph was generated between a homology model of acylP-bound *Sp*PlsY, constructed using the crystal structure of *Aa*PlsY (PDB entry 5XJ7) as the template, and the cryo-EM structure of the Gpatin-bound *Sp*PlsY complex. The substrates acyl-phosphate and glycerol 3-phosphate (green sticks) are superposed from PDB entries 5XJ7 and 5XJ6, respectively. Gpatin is shown as yellow spheres. Upon binding to the C-terminal transmembrane bundle (red), the N-terminal bundle (blue) swings away, disrupting the substrate-binding pocket and catalytic site. Membrane phospholipids (grey spheres) occupy the resulting gap between Gpatin and the N-terminal bundle, potentially restricting inhibitor diffusion back into the membrane.

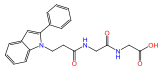
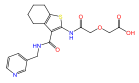
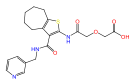
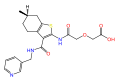
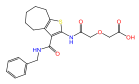
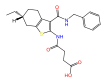
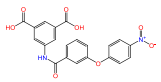
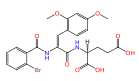
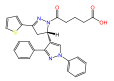
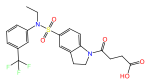
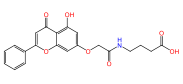
874 **Table S1. Screening**

| | No. | Code | Structure | Docking score[a] | Activity[b] (%) |
|---|---|---|---|---|---|
| **1st Screening** | | | | | |
| | Y1 | 0466-0064 |  | -13.233 | 83.7 |
| | Y2 | 0671-0223 |  | -10.818 | 99.9 |
| | Y3 | 0834-0004 |  | -12.270 | 98.2 |
| | Y4 | 1418-0043 |  | -12.163 | 89.7 |
| | Y5 | 2509-0042 |  | -15.294 | 93.5 |
| | Y6 | 2509-0070 |  | -12.999 | 100.6 |
| | Y7[c] | 2738-0364 |  | -13.230 | 39.1 |
| | Y8 | 2746-0341 |  | -10.661 | 92.0 |
| | Y9 | 3172-0799 |  | -13.623 | 51.6 |
| | Y10 | 3379-2706 |  | -13.094 | 86.7 |
| | Y11 | 3379-3157 |  | -12.973 | 118.1 |
| | Y12 | 3793-4510 |  | -13.076 | 70.7 |
| | Y13 | 4052-4417 |  | -12.421 | 109.0 |
| | Y14 | 4052-4509 |  | -11.765 | 55.9 |
| | Y15 | 4405-0931 |  | -14.018 | 98.6 |

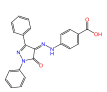
| | | | | |
|---|---|---|---|---|
| Y16 | 4488-1965 |  | -13.838 | 58.4 |
| Y17 | 4710-0021 |  | -16.445 | 88.9 |
| Y18 | 4896-4453 |  | -13.653 | 80.9 |
| Y19 | 4909-0086 |  | -11.487 | 85.6 |
| Y20 | 4909-0223 |  | -12.212 | 84.9 |
| Y21 | 4986-0947 |  | -12.402 | 86.8 |
| Y22 | 5267-1326 |  | -14.849 | 102.4 |
| Y23 | 5590-0068 |  | -13.721 | 94.8 |
| Y24 | 5625-0049 |  | -15.273 | 74.2 |
| Y25 | 5695-0543 |  | -13.063 | 87.9 |
| **Y26** | 5959-0169 |  | -12.090 | 38.8 |
| Y27 | 6193-0962 |  | -15.189 | 65.1 |
| **Y28** | 7202-3055 |  | -12.040 | 44.8 |
| Y29 | 8006-5480 |  | -12.378 | 90.3 |
| Y30 | 8007-8952 |  | -12.189 | 71.4 |
| **Y31** | 8011-4271 |  | -13.227 | 25.5 |
| Y32 | 8015-4227 |  | -12.892 | 84.1 |

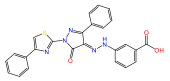
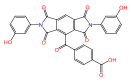
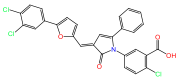
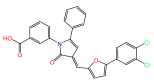
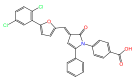
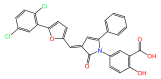
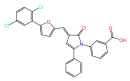
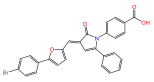
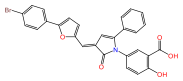
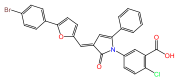
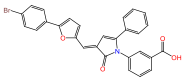
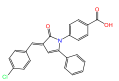
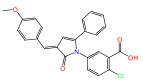
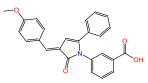
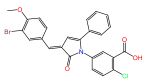
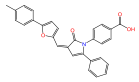
| | | | | |
|---|---|---|---|---|
| Y33 | 8019-8057 |  | -12.670 | 88.7 |
| Y34 | c090-0423 |  | -11.470 | 81.0 |
| Y35 | c090-0425 |  | -12.627 | 103.7 |
| Y36 | c090-0461 |  | -13.827 | 71.3 |
| Y37 | c090-0462 |  | -13.010 | 100.0 |
| Y38 | c090-0488 |  | -13.461 | 112.4 |
| Y39 | c200-2976 |  | -14.801 | 94.0 |
| Y40 | c327-0101 |  | -12.925 | 93.3 |
| Y41 | C327-0169 |  | -12.103 | 89.8 |
| Y42 | c337-0223 |  | -10.666 | 85.2 |
| Y43 | c563-0624 |  | -12.183 | 91.1 |
| Y44 | c683-0663 |  | -13.160 | 83.8 |
| Y45 | d008-0060 |  | -15.045 | 83.2 |
| Y46 | d715-0409 |  | -14.333 | 86.7 |
| Y47 | d715-0515 |  | -14.478 | 68.7 |
| Y48 | d715-0537 |  | -14.650 | 83.7 |
| Y49 | d715-2871 |  | -13.813 | 98.2 |

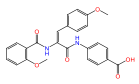
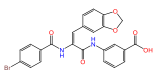
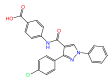
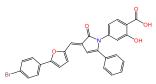
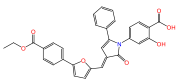
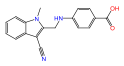
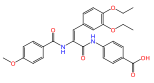
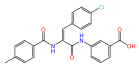
| | | | | |
|---|---|---|---|---|
| Y50 | e544-0129 |  | -14.023 | 76.6 |
| **Y51** | k065-0090 |  | -12.750 | 33.4 |
| Y52 | y040-8304 |  | -13.006 | 98.8 |
| Y53 | y040-8305 |  | -15.558 | 95.2 |
| Y54 | y040-8472 |  | -13.007 | 97.7 |
| Y55 | y040-8476 |  | -13.193 | 101.3 |
| Y56 | y040-8481 |  | -13.291 | 101.3 |
| Y57 | y040-8594 |  | -13.340 | 108.0 |
| Y58 | y040-8809 |  | -12.266 | 106.7 |
| Y59 | y040-8819 |  | -13.102 | 111.4 |
| Y60 | y040-8820 |  | -14.492 | 104.0 |
| Y61 | y041-1344 |  | -12.961 | 108.5 |
| Y62 | y041-1870 |  | -13.490 | 92.3 |
| Y63 | y041-1875 |  | -12.396 | 99.5 |
| Y64 | y041-2116 |  | -12.643 | 92.0 |
| Y65 | y041-2946 |  | -13.868 | 87.7 |
| Y66 | y041-3729 |  | -13.137 | 90.8 |

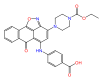
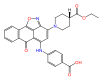
| | | | | |
|---|---|---|---|---|
| Y67 | y041-4101 |  | -13.430 | 92.3 |
| Y68 | y200-0350 |  | -12.562 | 94.3 |
| Y69 | y200-0366 |  | -13.163 | 93.5 |
| Y70 | y200-0371 |  | -13.047 | 106.8 |
| Y71 | y200-0407 |  | -12.202 | 102.7 |
| Y72 | y200-0430 |  | -12.424 | 90.4 |
| Y73 | y200-3779 |  | -12.636 | 98.6 |
| Y74 | y200-5909 |  | -13.356 | 98.1 |
| Y75 | 2036-1783 |  | -13.233 | 108.5 |
| Y76 | 2509-0031 |  | -16.578 | 91.6 |
| Y77 | 4488-1980 |  | -13.179 | 50.5 |
| Y78 | 4052-4508 |  | -12.217 | 51.8 |
| Y79 | 4557-0031 |  | -11.465 | 102.8 |
| Y80 | c563-0664 |  | -13.553 | 93.6 |
| Y81 | d715-1491 |  | -13.374 | 97.2 |

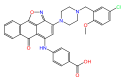
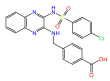
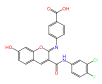
**2nd Screening**

| | | | | |
|---|---|---|---|---|
| **T1**[d] | 1652-2127 |  | -12.353 | 17.9 |

| | | | | |
|---|---|---|---|---|
| T2 | 1697-1286 |  | -12.241 | 59.8 |
| T3 | 1697-1592 |  | -11.302 | 73.6 |
| T4 | 2036-0800 |  | -13.030 | 101.9 |
| T5 | 2150-0020 |  | -11.095 | 64.2 |
| T6 | 2150-0039 |  | -11.268 | 95.9 |
| T7 | 2150-0082 |  | -9.744 | 73.0 |
| T8 | 2150-0085 |  | -11.918 | 52.3 |
| T9 | 2150-0105 |  | -11.311 | 75.1 |
| T10 | 2150-0146 |  | -9.349 | 68.5 |
| T11 | 2150-0149 |  | -13.009 | 59.0 |
| **T12** | 2150-0150 |  | -11.209 | 40.0 |
| T13 | 2150-0169 |  | -10.901 | 106.6 |
| T14 | 2150-0274 |  | -11.515 | 104.0 |
| T15 | 2150-0409 |  | -11.931 | 72.2 |
| T16 | 2150-0432 |  | -11.689 | 81.8 |
| T17 | 2150-0541 |  | -12.311 | 110.6 |
| T18 | 2150-1000 |  | -11.307 | 110.6 |

| | | | | |
|---|---|---|---|---|
| T19 | 3199-0273 |  | -10.317 | 57.5 |
| T20 | 3379-2181 |  | -12.423 | 106.7 |
| T21 | 3379-2240 |  | -11.583 | 87.4 |
| T22 | 3935-1400 |  | -11.478 | 50.9 |
| T23 | 3970-1625 |  | -11.912 | 67.1 |
| **T24** | 3970-1703 |  | -12.409 | 46.0 |
| T25 | 4237-0542 |  | -11.911 | 76.8 |
| T26 | 4358-4605 |  | -9.808 | 62.3 |
| T27 | 4896-4173 |  | -11.567 | 91.7 |
| T28 | 5590-0069 |  | -13.504 | 101.1 |
| T29 | 5613-0166 |  | -11.875 | 101.0 |
| T30 | 6197-5108 |  | -10.899 | 84.5 |
| T31 | 6197-5257 |  | -11.070 | 62.4 |
| T32 | 7229-1385 |  | -11.451 | 83.0 |
| T33 | 8001-3486 |  | -12.493 | 59.5 |
| T34 | C090-0398 |  | -13.350 | 64.0 |
| **T35** | C090-0407 |  | -13.967 | 48.6 |

| | | | | |
|---|---|---|---|---|
| T36 | C090-0410 |  | -9.442 | 71.1 |
| **T37** | C090-0411 |  | -11.138 | 32.4 |
| T38 | C090-0416 |  | -11.611 | 100.7 |
| **T39** | C090-0417 |  | -11.460 | 29.3 |
| T40 | C090-0419 |  | -11.708 | 69.1 |
| T41 | C090-0422 |  | -11.735 | 76.4 |
| T42 | C090-0424 |  | -11.821 | 108.5 |
| T43 | C090-0431 |  | -9.710 | 102.7 |
| **T44** | C090-0432 |  | -8.623 | 29.0 |
| T45 | C090-0434 |  | -12.894 | 114.6 |
| T46 | C090-0440 |  | -8.713 | 87.5 |
| T47 | C090-0441 |  | -11.487 | 54.9 |
| T48 | C090-0447 |  | -10.142 | 110.3 |
| T49 | C090-0449 |  | -12.969 | 90.6 |
| T50 | C090-0450 |  | -10.835 | 79.6 |
| T51 | C090-0458 |  | -9.509 | 101.3 |
| T52 | C090-0459 |  | -7.734 | 102.0 |

| | | | | |
|---|---|---|---|---|
| T53 | C090-0465 |  | -9.104 | 77.5 |
| T54 | C090-0467 |  | -11.966 | 62.7 |
| T55 | C090-0470 |  | -12.409 | 63.0 |
| **T56** | C090-0471 |  | -11.988 | 48.4 |
| **T57** | C090-0474 |  | -11.493 | 36.8 |
| T58 | C090-0477 |  | -11.047 | 106.3 |
| T59 | C301-7220 |  | -11.965 | 107.4 |
| T60 | C669-2612 |  | -10.875 | 99.8 |
| T61 | C683-0548 |  | -13.884 | 81.3 |
| **T62** | K078-0051 |  | -11.231 | 29.9 |
| T63 | K220-18544 |  | -11.369 | 64.7 |

[a]Glide-XP docking score. More negative values indicate stronger predicted binding; scores ≤ −10 are generally considered indicative of high-affinity interactions. [b] Residual SpPlsY activity measured in the presence of 20 μM compound. [c]Compounds exhibiting >50% inhibition are highlighted in red. [d]Gpatin.

880 **Table S1. Cryo-EM data collection and refinement statistics.**

881

| | ***Sp*PlsY** |
|---|---|
| **Data collection and processing** | |
| Magnification | 130 k |
| Voltage (kV) | 300 |
| Electron exposure ($e^-/Å^2$) | 50 |
| Defocus range (μm) | -2.2 to -1.2 |
| Pixel size (Å) | 0.934 |
| Symmetry imposed | *C*2 |
| Initial particle number | 5,856,796 |
| Final particle number | 141,306 |
| Map resolution (Å) | 2.61 |
| FSC threshold | 0.143 |
| **Refinement** | |
| Model resolution (Å) | 2.80 |
| FSC threshold | 0.5 |
| Map sharpening *B* factor ($Å^2$) | -89.8 |
| **Model composition** | |
| Non-hydrogen atoms | 3,494 |
| Protein residues | 412 |
| Ligands | 8 |
| *B* factor ($Å^2$) | |
| Protein | 79.56 |
| Ligand | 97.27 |
| R.m.s. deviations | |
| Bond lengths (Å) | 0.011 |
| Bond angles (°) | 1.333 |
| Validation | |
| MolProbity score | 2.46 |
| Clashscore | 8.07 |
| Ramachandran plot | |
| Favored (%) | 98.02 |
| Allowed (%) | 1.98 |
| Outliers (%) | 0.00 |

882

## Supplementary Files

This is a list of supplementary files associated with this preprint. Click to download.

- movie.mp4